The cut material gathered for the different cutting depths show similar grain sizes. The cutting force signal at 4 mm cutting depth implies chips that are formed but the material gathered has almost no chips. This is dissimilar to the sandstone where numerous chips were present. These small chips is a significant problem for cleaning operations in underground stopes and it has been reported this is a key reason why mechanical mining of the UG2 reef does not work.

This also implies that more fine fragmentations will occur which is not good in underground mining environments.

Figure 4.22 shows the specific energy at 2 mm and 4 mm cutting depth and different s/d values.

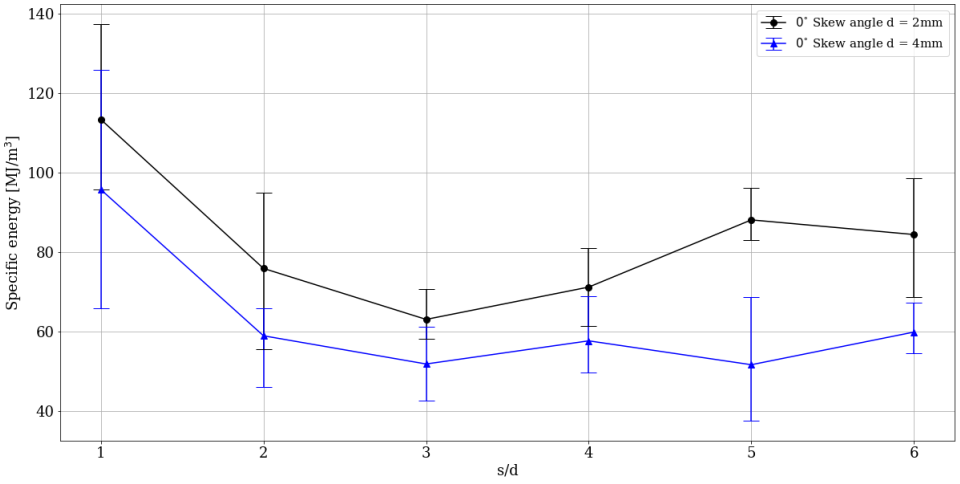

Figure 4.22: Specific energy at 2 mm and 4 mm cutting depth and different s/d values.

Figure 4.22 shows that there is a difference in the trend of the specific energy at different cutting depths. But there are similarities to the results obtained for the sandstone shown in section 3.3.1. In both cases the deeper the cut, the lower the specific energy for the different s/d values.

Both cutting depths show that an optimal s/d value is 3 when the skew angle is zero. But at a cutting depth of 4 mm the cutting depth plateaus at a s/d of 4. This was the same for the normal forces and drag forces.

4.3 Comparison between cutting of UG2 and sandstone

In this section comparisons will be made between the results obtained from the cutting tests of the sandstone and the UG2 reef samples.

The variance in strength on a millimetre scale of the rock samples were compared. When looking at the cutting data the following was observed.

As an indication of the variance in strength on a millimetre scale of the sample a colour map was made of the mean force for all 18 runs. Figure 4.25 is an extract of the colour map, where the y-axis is the number of the run, the run number in the cutting sequence as discussed in section 3.3 and shown in figure 3.14b, and on the x-axis is the cutting distance. The colour map represents the surface of the rock sample, the same as figure 3.14b. The colour map shows how the cutting forces change per run and where more force was required to make a cut on the surface of the rock sample. The cutting distance is 150 mm. The cut is from left to right. The runs either starts at the top or at the bottom depending on the direction of the cut sequence as discussed in section 3.3.1. Figure 4.23 shows an enlarged example of the y-axis from run 1 to run 9 where the cutting sequence runs from top to bottom.

In the appendix there are enlarged images of all the colour maps.

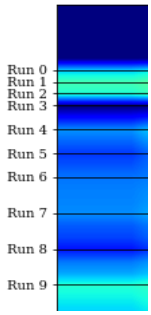

Figure 4.23: The run sequence on the colour map.

To map the force the data of the 150 mm is divided into 12 sections. The mean of each section is then mapped. The mapping use a bi-linear interpolation. Figure 4.24 shows how the force signal of 150 mm is divided into 12 sections and the mean taken for each section. For the mapping the orange line will be mapped.

Figure 4.24 is the normal force signal for cutting sandstone at 2 mm of cutting depth, skew angle of zero and s/d of 3.

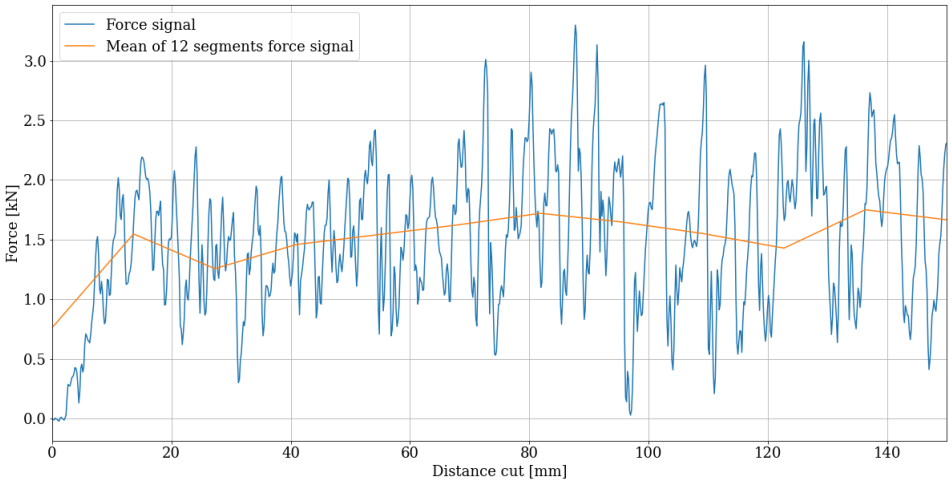

Figure 4.24: Changing the force signal to mapping signal.

Sandstone and UG2 is compared at a cutting depth of 2 mm and different skew angles. The mapping of both the drag force and side force is compared. From the comparison a conclusion can be made of how variance in strength on a millimetre scale of the rock changes, for these scaled tests.

Figure 4.25 shows the drag force map for cutting sandstone at 2 mm cutting depth with skew angle 0°.

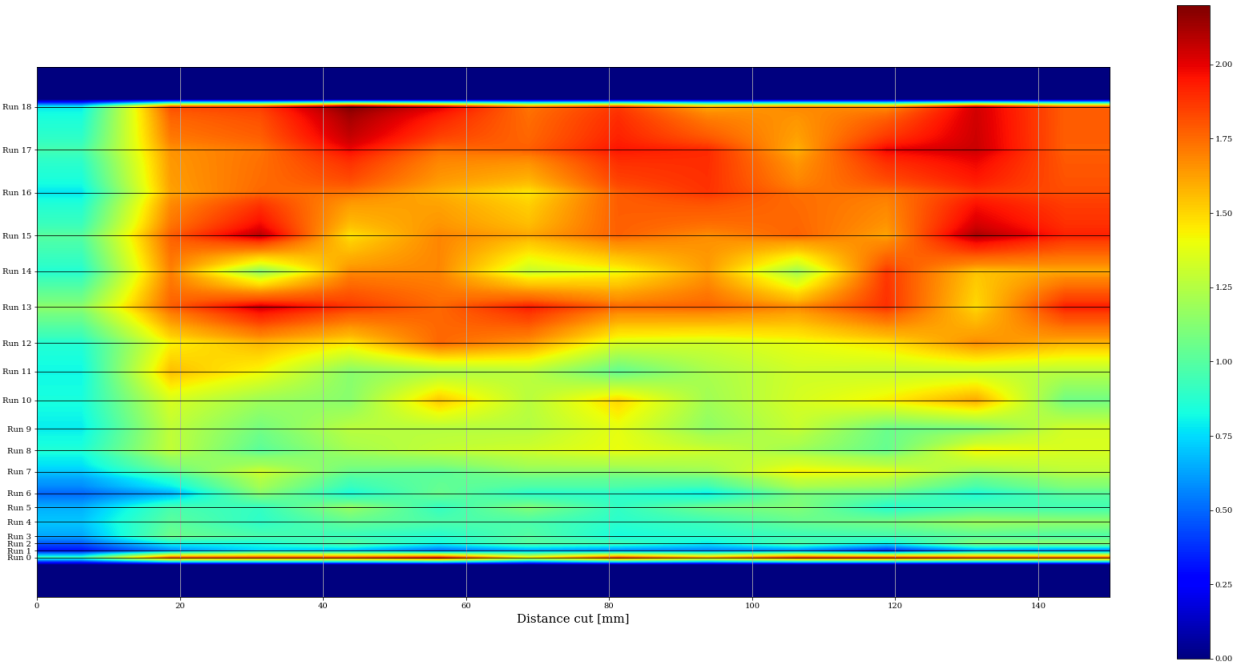

Figure 4.25: Drag force mapping of sandstone at skew angle = 0°.

Figure 4.25 show that the colour remains fairly consistent per run. Thus, the sandstone has little to no variance in strength on a millimetre scale. The figure also shows how the mean drag force increases from run 1 to run 18, from bottom to top. This is the same for negative and positive skew angle as

shown in the appendix. For the first 10 mm of the cut the mean drag force is low, this is due to the cut initiating. This is clear when looking at the first 10 mm of cut in figure 4.24.

Figure 4.26 shows the drag force map for cutting UG2 at 2 mm cutting depth with a skew angle 0°.

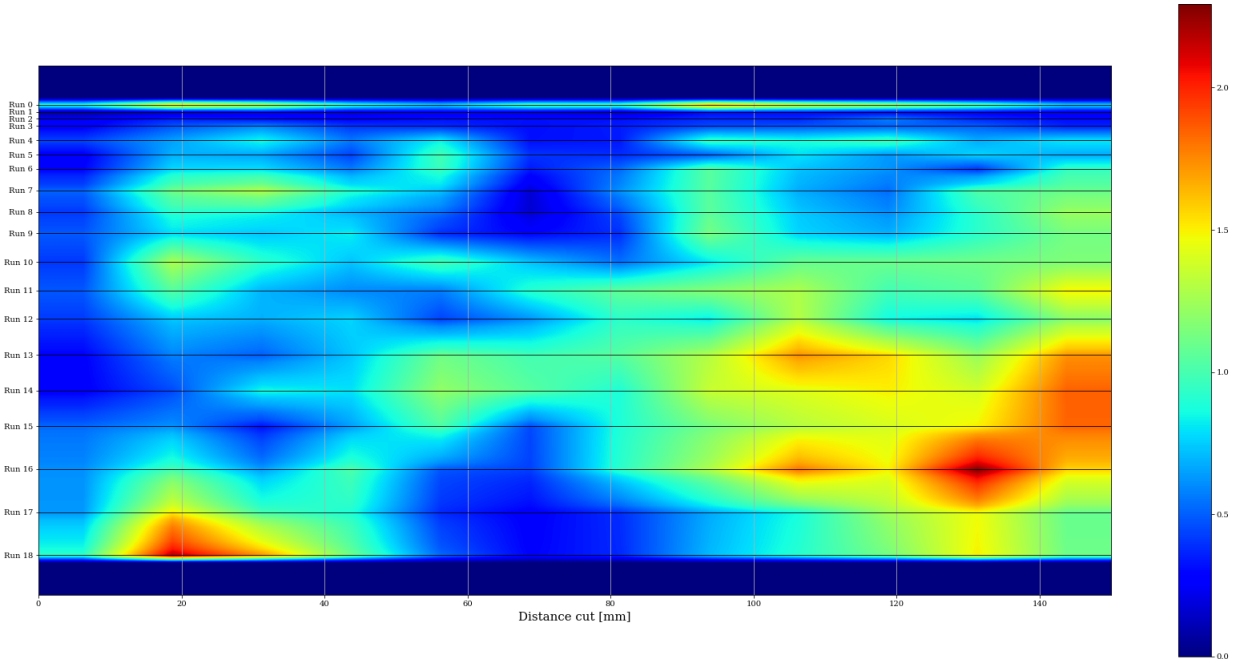

Figure 4.26: Drag force mapping of UG2 at skew angle = 0°.

Figure 4.26 show that the colour per run is much less consistent than for sandstone. This implies that the rock sample has large variance in strength on a millimetre scale. The appendix shows an enlarged colour map for zero skew angle, positive skew angle and negative skew angle when cutting UG2 reef samples.

When comparing the figures, 4.26 to 4.26, its seems that there are certain parts of the rock sample where the inconsistencies are. To show this better the same mapping was used but the mean of the section was divided by the mean of the run. This shows where in each run there were low and high forces compared to the mean of the run.

Figure 4.27 shows the normalized drag force map for cutting UG2 at 2 mm cutting depth with skew angle 0°.

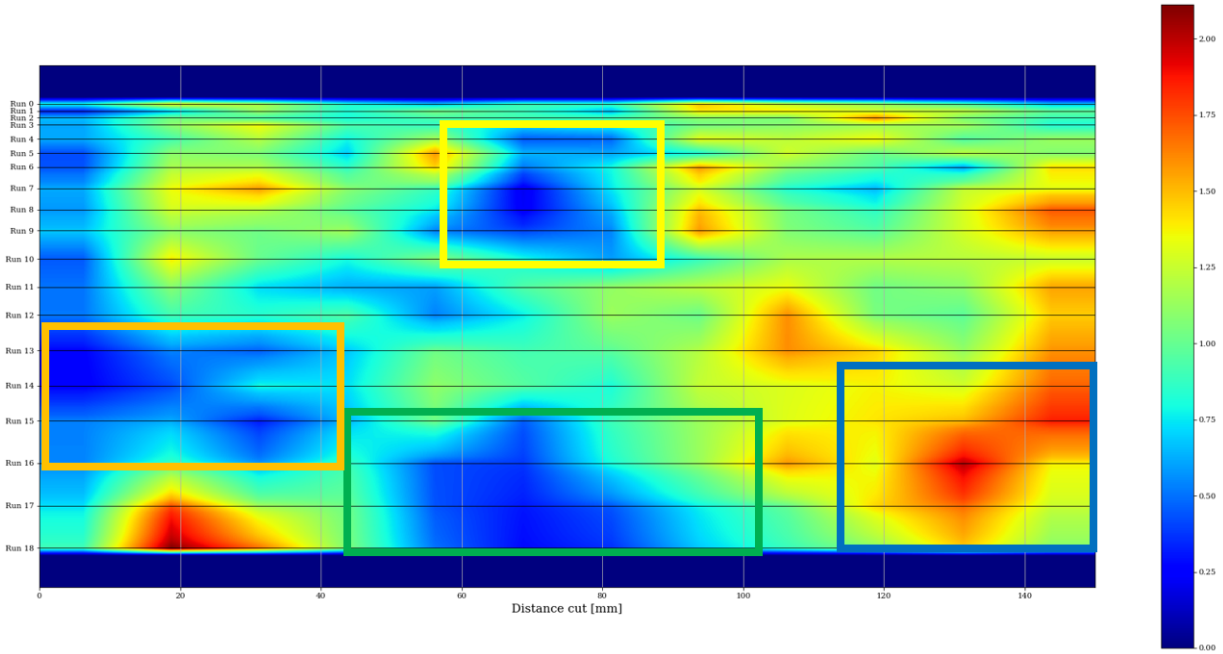

Figure 4.27: Normalized drag force mapping of UG2 at skew angle = 0°.

Figure 4.28 shows the normalized drag force map for cutting UG2 at 2 mm cutting depth with skew angle −10°.

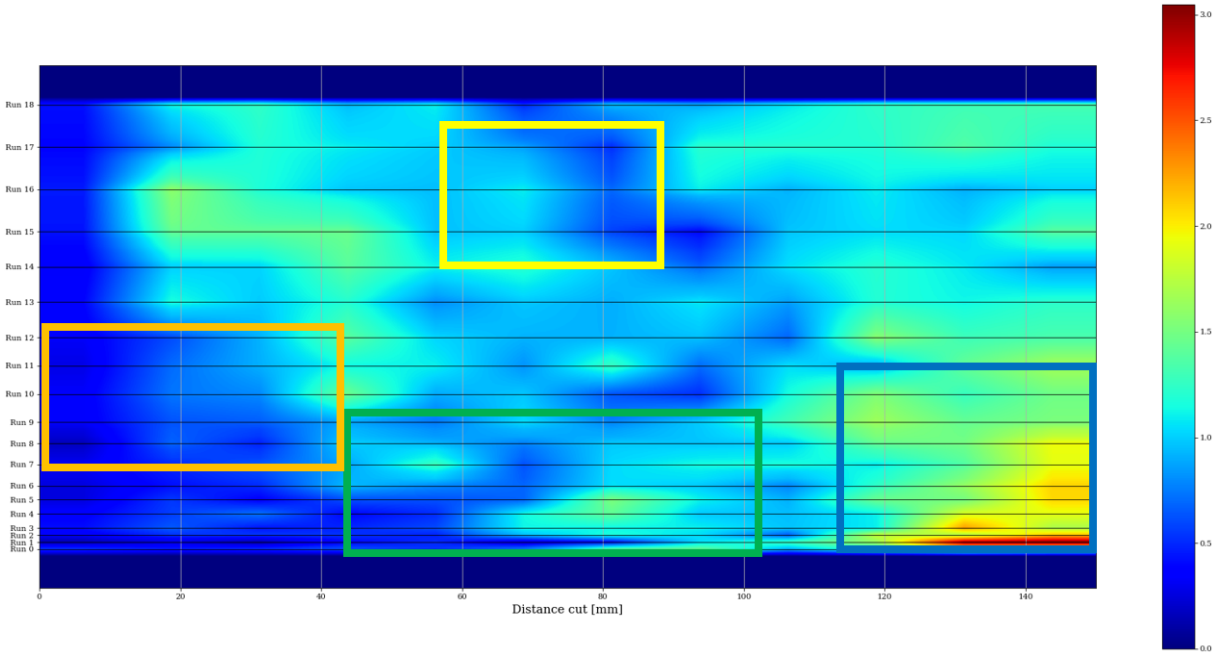

Figure 4.28: Normalized drag force mapping of UG2 at skew angle = −10°.

Figure 4.29 shows the normalized drag force map for cutting UG2 at 2 mm cutting depth with skew angle +10°.

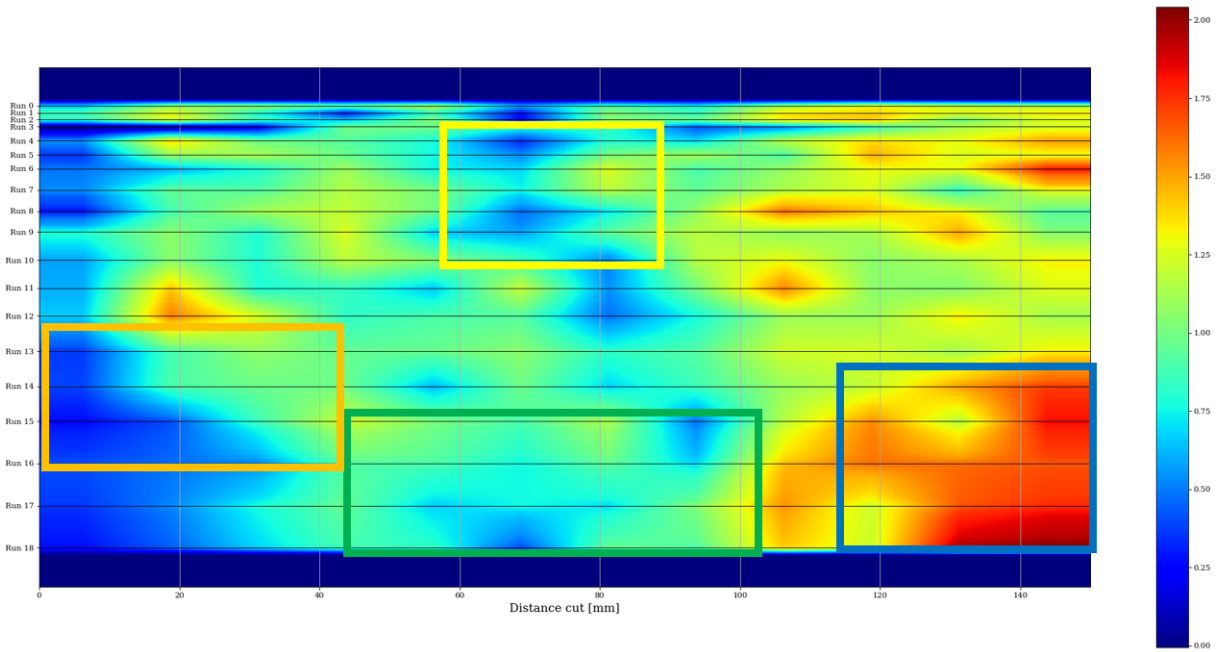

Figure 4.29: Normalized drag force mapping of UG2 at skew angle = $+10^{\circ}$.

The normalized maps show that there is an inconsistency in the lower middle of the rock sample shown by the green boxes. This inconsistency is in all three cutting sequences. It is assumed that the rock is weaker at this point due to the lower force required to cut the rock.

There are two other inconsistencies where it is assumed the rock is softer. One is at the start of the cut, between 0 mm to 40 mm, shown by the orange boxes. The other is shown by the yellow boxes. The lower right corner is assumed to be stronger than the rest due to the required force being higher than the mean, shown by the blue boxes.

The normalized colour maps clearly show that the UG2 rock sample has large variance in strength on a millimetre scale. Thus, the sample will cause more variance in the cutting data. This can be seen in the variance in the cutting data shown in section 4.2.

Figure 4.30 shows the drag force signal for cutting sandstone at 2 mm cutting depth, skew angle of zero and s/d of 6. The drag force signal is run 18 in figure 4.26.

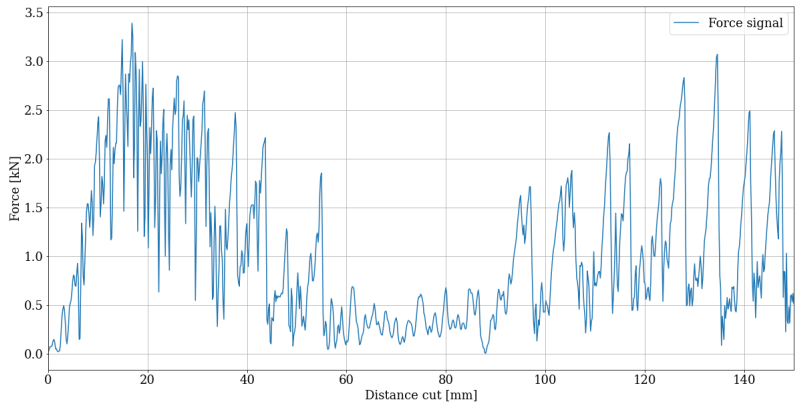

Figure 4.30: Drag force signal for cutting UG2 at 2 mm cutting depth, skew angle of zero and s/d of 6.

The figure shows how the required drag force decreases between 60 mm to 90 mm. This is the area where the inconsistency is in the rock sample.

Figure 4.31 shows the side force map for cutting sandstone at 2 mm cutting depth with skew angle 0°.

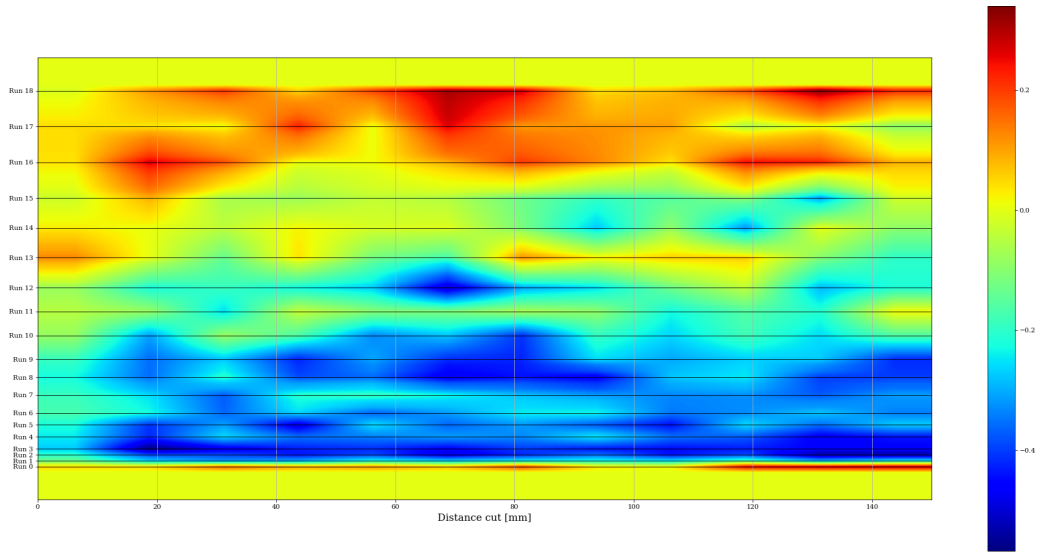

Figure 4.31: Side force mapping of sandstone at skew angle = 0°.

Figure 4.32 shows the side force map for cutting sandstone at 2 mm cutting depth with skew angle −10°.

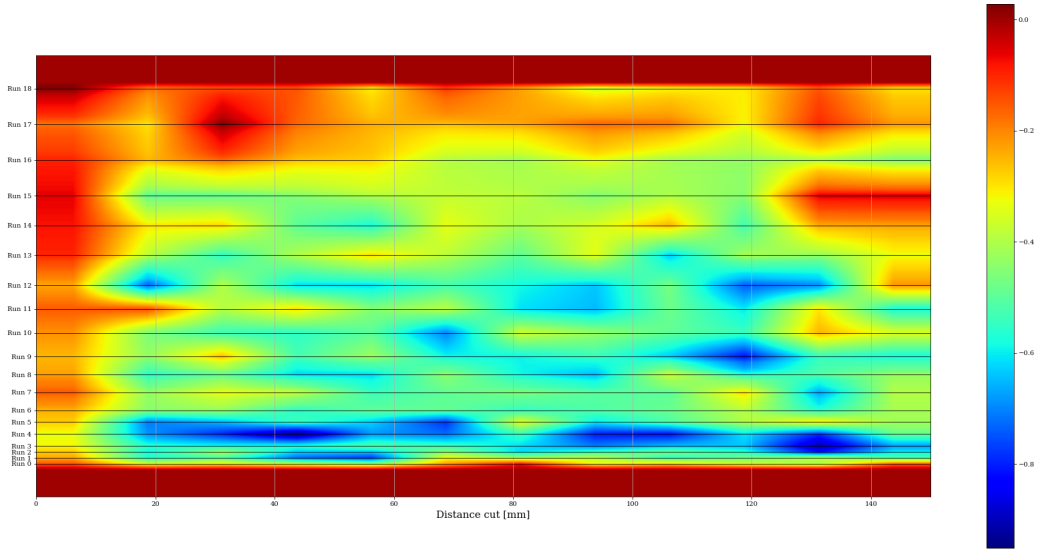

Figure 4.32: Side force mapping of sandstone at skew angle = -10°.

Figure 4.33 shows the side force map for cutting sandstone at 2 mm cutting depth with skew angle $+10^{\circ}$.

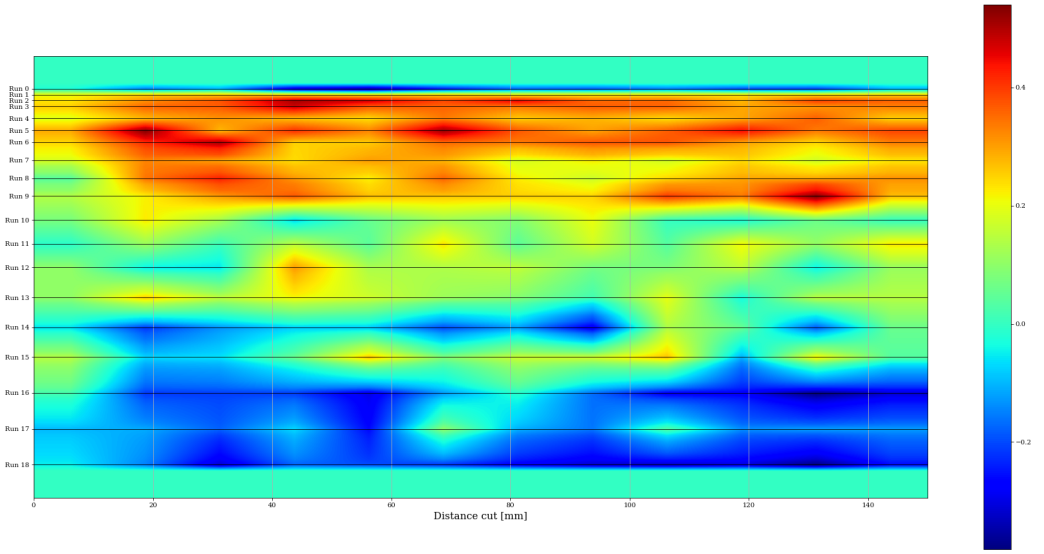

Figure 4.33: Side force mapping of sandstone at skew angle = $+10^{\circ}$.

Figures 4.31 to 4.32 show the same as figure 4.25. The maps show how the magnitude of the side force decreases as the number of the run increases.

Figure 4.32 shows between a s/d of 4 to 5, run 10 to 15, The side force is almost zero and that the direction of the side force changes at that range of s/d values. This was also shown in section 4.2.

Figure 4.34 shows the side force map for cutting UG2 at 2 mm cutting depth with skew angle 0°.

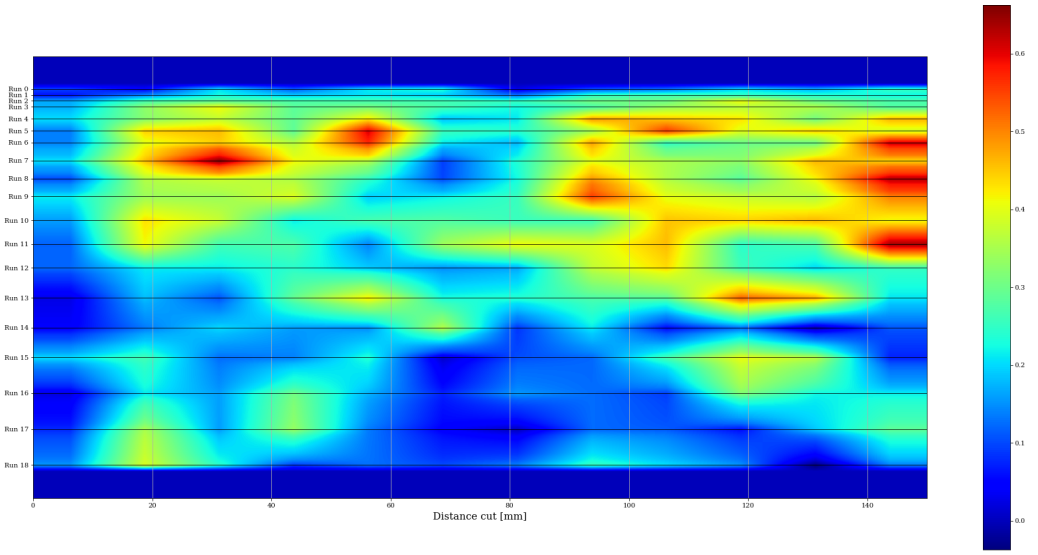

Figure 4.34: Side force mapping of UG2 at skew angle = 0°.

Figure 4.35 shows the side force map for cutting UG2 at 2 mm cutting depth with skew angle $-10°$.

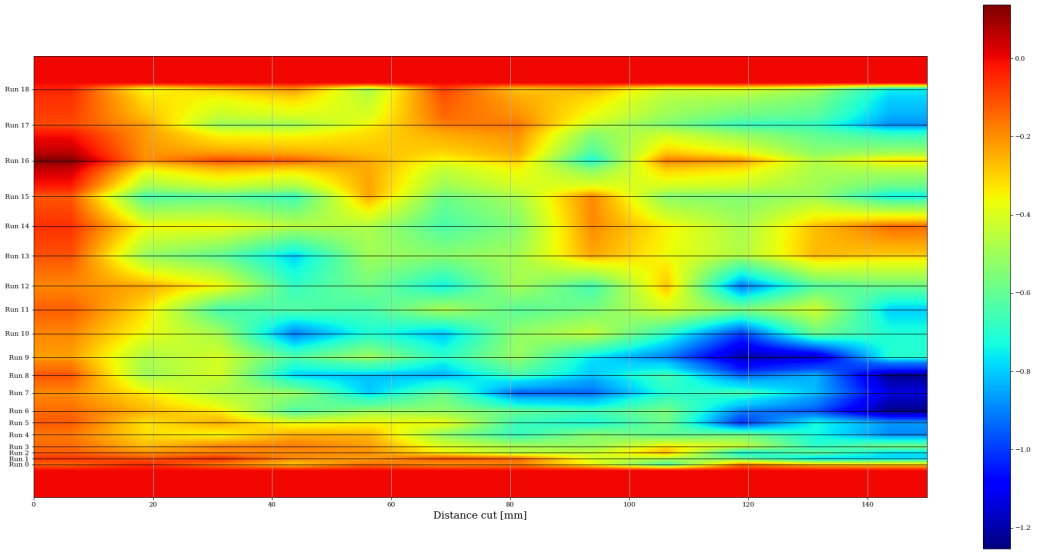

Figure 4.35: Side force mapping of UG2 at skew angle = $-10°$.

Figure 4.36 shows the side force map for cutting UG2 at 2 mm cutting depth with skew angle $+10°$.

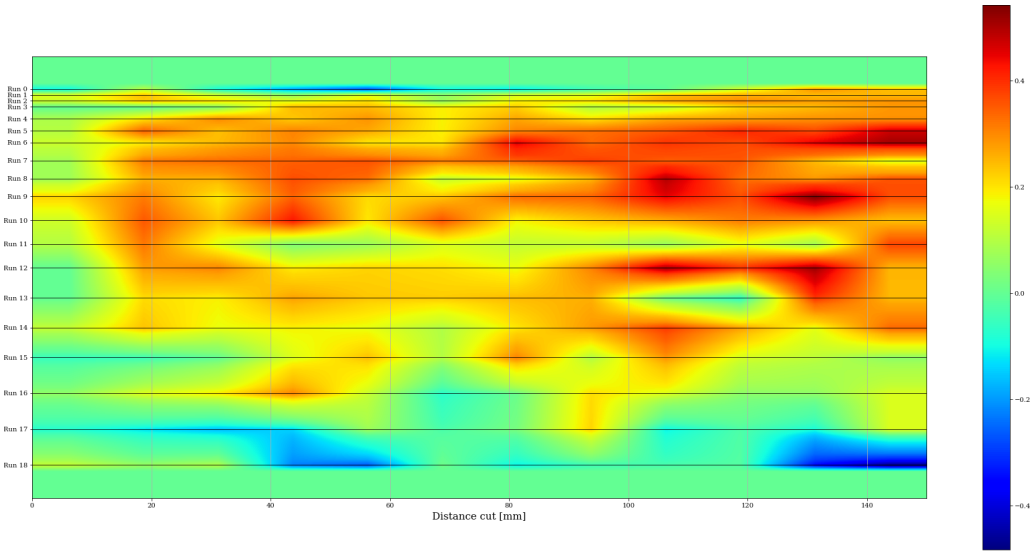

Figure 4.36: Side force mapping of UG2 at skew angle = $+10°$.

Figures 4.34 to 4.32 show the same as figure 4.26. The maps show that the UG2 reef sample has large variance in strength on a millimetre scale.

An FFT analysis was performed on the drag force signal data, of both the sandstone and the UG2, to emphasise the periodic nature of the data. For both cases, three initial runs where investigated, for a cutting depth of 2 mm and a cutting depth of 4 mm, and a skew angle of zero. For the FFT the original drag force data was used, not the mean data used to plot the colour maps.

Figure 4.37 shows the results of the FFT analysis of the drag force signal for sandstone at a cutting depth of 2 mm. The horizontal axis shows the number of drag force signal peaks per cut mm.

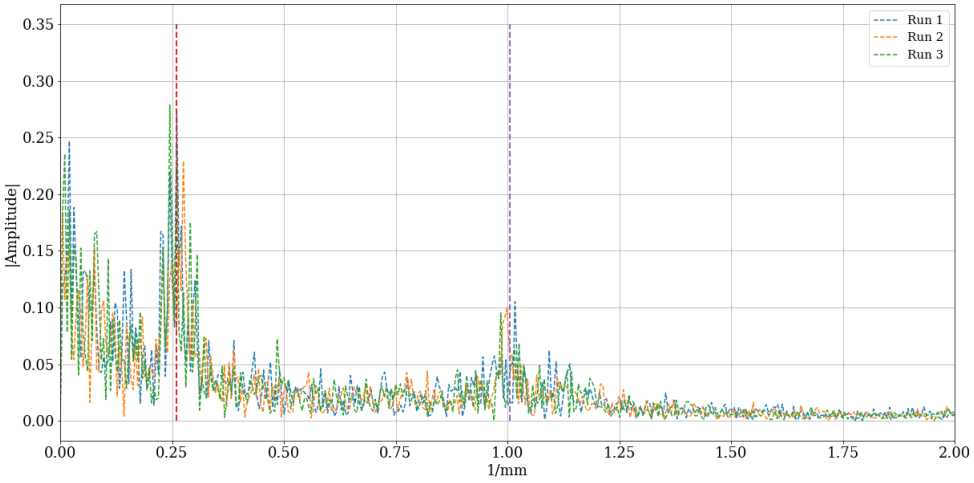

Figure 4.37: FFT analysis of the drag force signal for sandstone at a cutting depth of 2 mm.

Figure 4.37 shows that there are two peaks. One shown by the red line at 0.25 $\frac{1}{mm}$ and the other

shown by the purple line at 1 $\frac{1}{mm}$.

Figure 4.38 shows the results of the FFT analysis of the drag force signal for sandstone at a cutting depth of 4 mm.

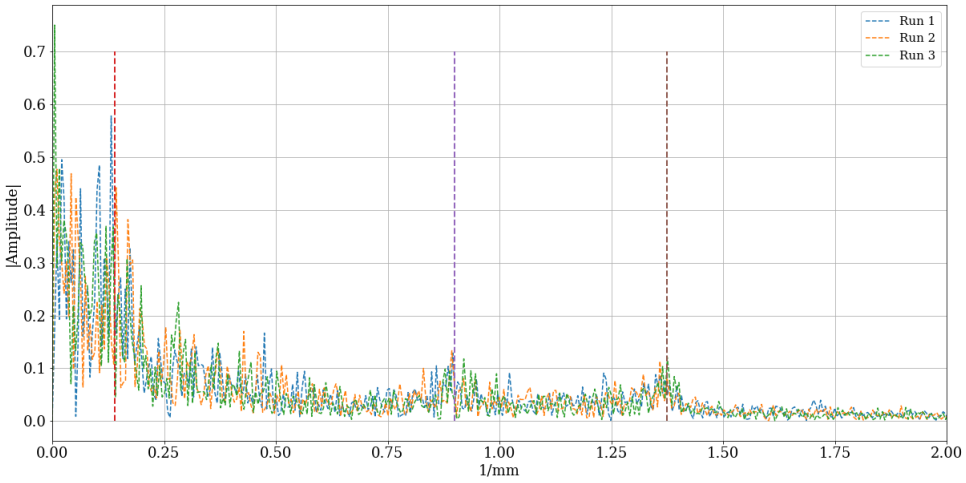

Figure 4.38: FFT analysis of the drag force signal for sandstone at a cutting depth of 4 mm.

Figure 4.38 shows that there are three peaks. One shown by the red line at 0.14 $\frac{1}{mm}$, another shown by the purple line at 0.9 $\frac{1}{mm}$ and the last shown by the brown line at 1.375 $\frac{1}{mm}$.

It is clear from figures 4.37 and 4.38 that the drag force signals for cutting sandstone are periodic.

The peaks also relate to the size of the chips formed. For a cutting depth of 2 mm the first peak is at 0.25 cycles/mm and for a cutting depth of 4 mm the first peak is at 0.14 cycles/mm. One can assume that the number of cycles per mm is linked to the number of chips formed per mm cut. So a cutting depth of 4 mm leads to larger chips. This is indeed the case when looking at the chips formed for the different cutting depths, as shown in figures 3.36a and 3.36b. The higher peaks represent smaller chips which seem to readily break down to powder.

Figure 4.39 shows the results of the FFT analysis of the drag force signal for UG2 at a cutting depth of 2 mm.

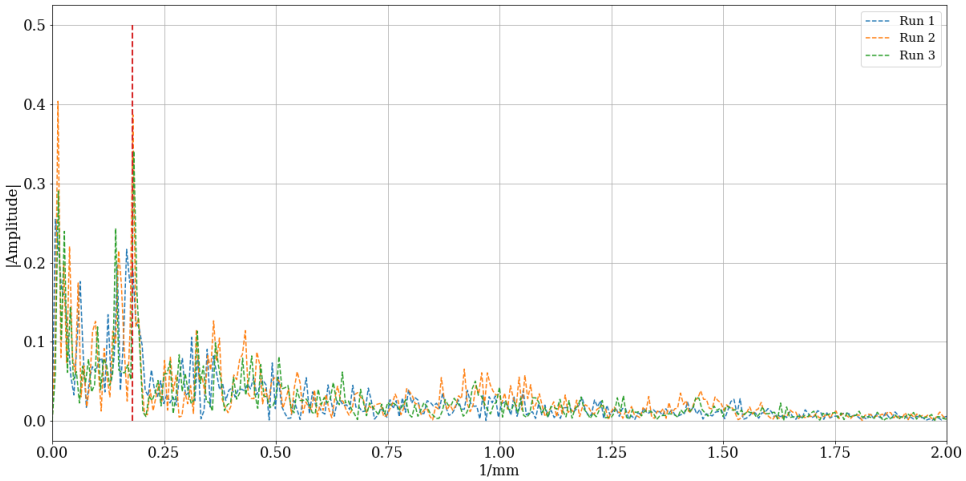

Figure 4.39: FFT analysis of the drag force signal for UG2 at a cutting depth of 2 mm.

Figure 4.39 shows that there is one peak shown by the red line at 0.18 $\frac{1}{mm}$.

Figure 4.40 shows the results of the FFT analysis of the drag force signal for UG2 at a cutting depth of 4 mm.

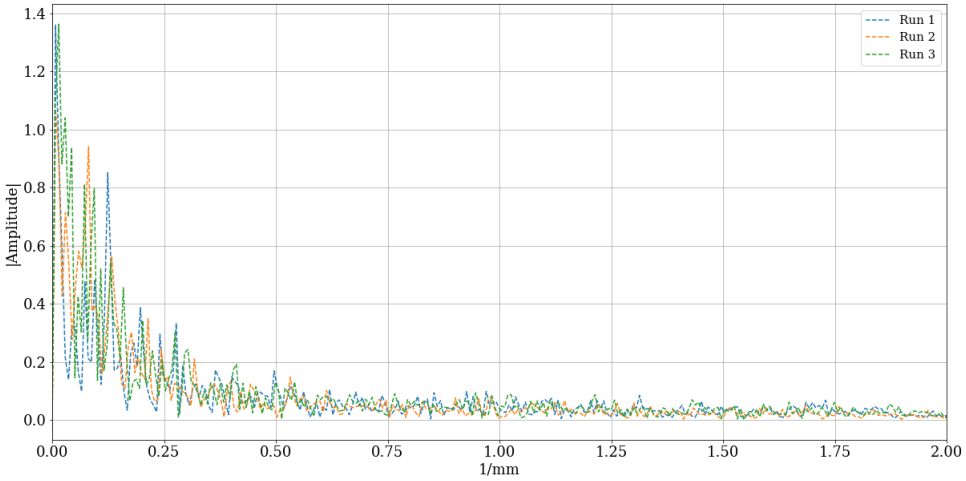

Figure 4.40: FFT analysis of the drag force signal for UG2 at a cutting depth of 4 mm.

Figure 4.40 shows no peaks when cutting UG2 at a cutting depth of 4 mm.

Figures 4.39 and 4.40 show that the drag force signal, when cutting UG2, is less periodic than sandstone. This is consistent with the fact that UG2 does not display the same period chip forming process as the sandstone.

The reason why the drag force signal, when cutting UG2, is not periodic is because of the UG2

having large variance in strength on a millimetre scale. The fact that the UG2 has this variance causes the cutting force required to vary with the inconsistency in the material, as shown by figure 4.30. Therefore causing the cutting force to not be periodic. The FFT should represent the size of the chips formed, as is for the sandstone, but for UG2 it is not the case.

But general conclusions are still clear. The maps show how the side force decreases as the run number increases. This is the same as the sandstone.

Figure 4.36 shows that the side force changes direction, same as the sandstone, but just at a larger s/d value. This is confirmed when looking at side force data is section 4.2.

In conclusion, for the comparison, between the cutting of sandstone and the cutting UG2 reef samples, the results show that there are some similar trends between the results obtained, but there are also various inconsistencies.

The force signals are similar when looking at the cutting depths. For 2 mm of cutting depth both samples have impulsive force signals and for 4 mm cutting depth the force signals are saw tooth.

The sandstone generates larger chips at a cutting depth of 4 mm whereas the UG2 causes almost no chip forming. This will cause more finer fragmentation that is undesirable in underground mines.

The mean normal force and drag force, for both rock samples at a cutting depth of 2 mm, follow the same trend where the mean force increases linearly as the s/d value increases. But the peak forces do not follow the same trend. The peak forces for the sandstone increase linearly like the mean force whereas the peak forces for the UG2 reef sample plateaus at a s/d value of 3.

At a cutting depth of 4 mm the mean forces, normal forces and drag forces, for the UG2 reef samples plateaus, which is unlike to the mean force results from cutting sandstone.

For both rock samples the mean and peak side forces follow the same trends.

When looking at the specific energy the UG2 reef sample plateaus at a s/d of 5 for a cutting depth of 2 mm and at a s/d of 4 for a cutting depth of 4. The specific energy of the sandstone does not plateau for any of the tested s/d values. But the optimal s/d values for both rock samples are similar for the respected cutting parameters.

Finally, the sandstone has little to no variance in strength on a millimetre scale whereas the UG2 reef sample Has large variance in strength on a millimetre scale. This introduces more variance in the data obtained from the UG2 reef sample.

4.4 Numerical simulation results

In this section the numerical simulation is compared to cutting results from three initial cuts, no influence of previous cuts, at 2 mm cutting depth and at 4 mm cutting depth with a skew angle of zero. Table 4.2 shows the data that will be used to compare the experimental results to the numerical simulation results.

Table 4.2: Experimental cutting data for UG2 at 2 mm and 4 mm cutting depth.

Cutting depth	FN [kN]	FD [kN]	FN' [kN]	FD' [kN]	FN'/FN	FD'/FD	FN/FD
2 mm	1.25	1	3.83	3.15	3.064	3.15	1.25
4 mm	3.8	3.01	11.24	8.91	2.96	2.96	1.26

Table 4.3 shows the maximum error value and the maximum percentage error for the results of the experimental cutting forces compared to the mean of the three runs.

Table 4.3: Maximum error for experimental runs.

Cutting depth	FN error value [kN]	FN error %[kN]	FD error value [kN]	FD error %[kN]	FN' error value [kN]	FN' error %[kN]	FD' error value [kN]	FD' error %[kN]
2 mm	0.2	16.32	0.16	15.52	0.2	5.21	0.24	7.54

The force signals for the cutting data in table 4.2 are shown in figures 4.41 to 4.44. The figures show the normal force and the drag force for the three cuts as well as the mean force and the peak force per cut.

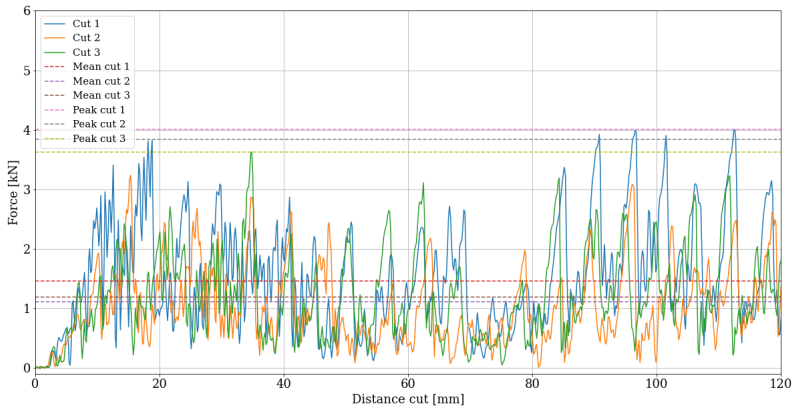

Figure 4.41: Normal force cutting signals for 2 mm cutting depth and skew angle of zero.

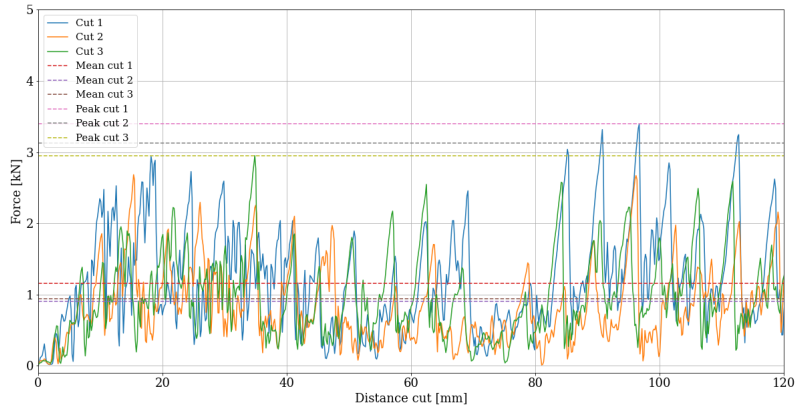

Figure 4.42: Drag force cutting signals for 2 mm cutting depth and skew angle of zero.

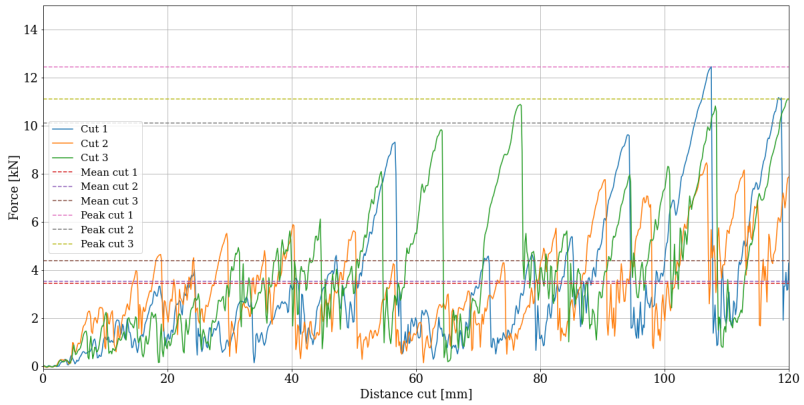

Figure 4.43: Normal force cutting signals for 4 mm cutting depth and skew angle of zero.

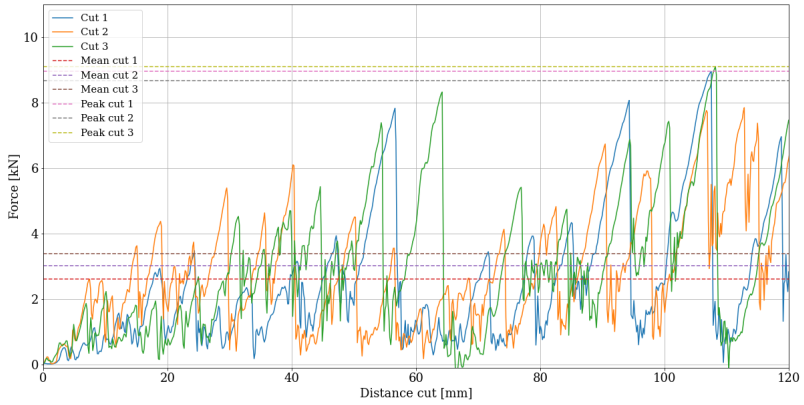

Figure 4.44: Drag force cutting signals for 4 mm cutting depth and skew angle of zero.

The numerical set-up that was selected for the final simulations was determined from the knowledge that was obtained from section 2.3. The set-up requiered the selection of various parameters, namely

element size, mesh type, boundary conditions and model parameters. All the parameters and material properties were updated through trial and error so that the results of the numerical simulation match the results from the laboratory scale cutting tests at a depth of 2 mm, as shown in table 4.2. The parameters for the CSCM were updated by changing the material properties, used in the equations given by (Novozhilov, Dmitriev and Mikhaluk, 2022) as discussed in section 2.2. The parameters were chosen to accurately predict the cutting forces at a cutting depth of 2 mm, then the same model with the same parameters were used at a cutting depth of 4 mm to determine if the model extrapolates accurately.

Section 2.3 showed that the element size had the largest impact on the peak force to mean force ratio. From table 4.2 a peak to mean force ratio of 3 is required. Thus an element size of 1.6 mm was used.

Owing to the mesh type not having a large impact on the final result, a tetrahedron mesh was selected. A tetrahedron mesh was selected due to (Jaime, 2011) recommending that a tetrahedron mesh will give a more realistic fracture pattern.

Figure 4.45 shows the model set-up for the numerical simulation. The figure shows the side view and the 3D view of the model set up.

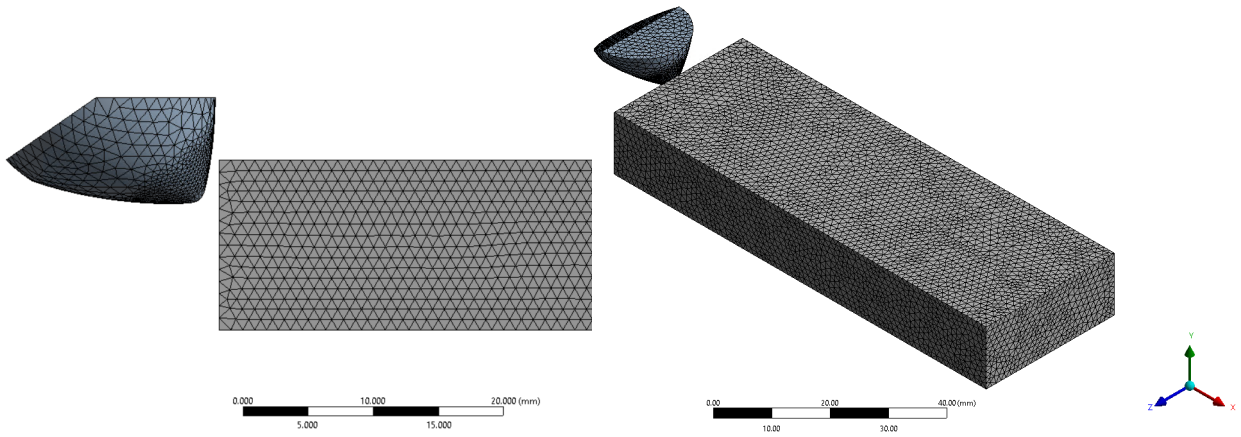

(a) Side view of model set up. **(b)** 3D view of model set-up.

Figure 4.45: Model set-up for numerical simulation for UG2 reef.

For the numerical simulation both side faces, bottom face and the back face were fixed. The front face was fixed in the z direction.

For the `ERODING_SURFACE_TO_SURFACE` all three parameters, the viscous damping coefficient, contact penalty scale factor and the target penalty scale factor, were selected as 5. This was selected because the penalty value did not have a large impact on the final simulation results as shown in section 2.3.

The friction coefficient and the dynamic coefficient had an influence on the ratio of normal force to

drag force as shown in section 2.3. Through trail and error a friction coefficient of 0.004, a dynamic coefficient of 0.001 and a decay constant of 1 was used.

Table 4.5 shows the model parameters that were used for the final numerical simulation. Equations from Novozhilov et al. (2022) were used to determine the CSCM parameters. Table 4.4 shows the material properties used in the equations of Novozhilov et al. (2022). These values of the material parameters fall in the range of values of UG2 reef samples. The aggregate size was chosen as the default value used by the CSCM.

Table 4.4: UG2 reef material parameters used in equations of Novozhilov et al. (2022).

Young's modulus [GPa]	Poisson's ratio	Density [g/cm^3]	Uniaxial compressive strength [MPa]	Aggregate size [mm]
83.2	0.152	4.19	70	19

Table 4.5: CSCM parameters for final numerical simulation.

CSCM parameters					
Control factors			Rate effects		
ρ	4.19	g/cm^3	η_{c0}	0.0006	
NPLOT	1.00		N_c	0.781	
INCRE	0.00		η_{t0}	0.0001	
IRATE	1.00		N_t	0.48	
ERODE	1.10		*overc*	58.1299	
RECOV	1.00		*overt*	58.1299	
IRETRC	1.00		S_{rate}	1	
PRED	0.00		*repow*	1	
Shear surface hardening			Stiffness		
N_H	0.00		G_0	3611.1	MPa
C_H	0.00		K_0	3984.7	MPa
Damage			Yield surface		
b	100		α	24.741	MPa
d	0.1		θ	0.3115	
G_{fc}	12.173	MPa·mm	λ	16.4444	MPa
G_{ft}	0.1217	MPa·mm	β	0.012	MPa^{-1}
G_{fs}	0.1217	MPa·mm	α_1	0.82	
pwrc	5		θ_1	0	MPa^{-1}
pwrt	1		λ_1	0.2407	
pmod	0		β_1	0.0058	MPa^{-1}
			α_2	0.76	
			θ_2	0	MPa^{-1}
			λ_2	0.76	
			β_2	0.0051	MPa^{-1}
Cap Geometry and hardening					
R	1.9537				
X_0	149.527	MPa			
W	0.065				
D_1	0.0006	MPa			
D_2	0	MPa^2			

Tables 4.6 and 4.7 show the results obtained for the numerical simulations at a cutting depth of 2 mm

and 4 mm. The tables also show the percentage error between the numerical simulation results and the experimental results.

Table 4.6: Numerical simulation force results for UG2 reef.

Cutting depth	FN	% Error	FD	% Error	FN'	% Error	FD'	% Error
2 mm	1.128	9.76	1.11	11.06	3.346	12.63	3.282	3.45
4 mm	1.408	62.94	1.837	38.94	4.718	58.02	5.652	36.56

Table 4.7: Numerical simulation ratio results for UG2 reef.

Cutting depth	FN'/FN	% Error	FD'/FD	% Error	FN/FD	% Error
2 mm	2.96	5.82	2.96	3.55	1.016	18.75
4 mm	3.35	13.2	3.07	3.95	0.766	39.17

The results in the tables show that the model parameters can be updated through trial and error to give similar results as the experimental results. But this only works when editing the model parameters so that the numerical simulation results are similar to the results for one set of experimental cutting parameters, in this case a cutting depth of 2 mm.

For the 2 mm cutting depth the percentage error for the force values are acceptable when compared to the percentage error in table 4.3. Thus, the numerical simulation set-up can be edited so that acceptable results are obtained. When using the same model set-up for a cutting depth of 4 mm, as used for the 2 mm cutting depth, the results are less than ideal as indicated by the percentage errors shown in 4.6.

This inability to generate the model parameters to be applicable to a large range of cutting parameters, has also been observed by other researchers in previous work (Huang et al., 2016; Jaime, 2011). It was assumed the error when changing cutting depth was due to poor modelling of the cutting tool. But after the results of the numerical simulations were obtained it is clear that the error is due to other factors.

The results in table 4.7 show that the ratios of peak force to mean force for both the normal force and the drag force, are close to 3, which is the same as the experimental results. This ratio was obtained by changing the element size. In section 2.3 it was shown that the peak force for the different element sizes remained similar but as the element size decreased the mean force increased. Thus, the material properties were updated so that the peak forces are similar and then the element size was edited to get the correct ratio. The peak force to mean force ratio is acceptable for both cutting depths.

Lastly this study, consider the ratio of the mean normal force to the mean drag force. Previous researchers also experienced a problem to get this ratio correct (Huang et al., 2016; Su and Akcin, 2011; Van Wyk et al., 2014). The contact parameters are important factors that change the ratio as well as element size. This ratio does not have a acceptable accuracy.

Figure 4.46 shows the normal force signals for the three numerical simulation runs at a cutting depth of 2 mm and a skew angle of zero.

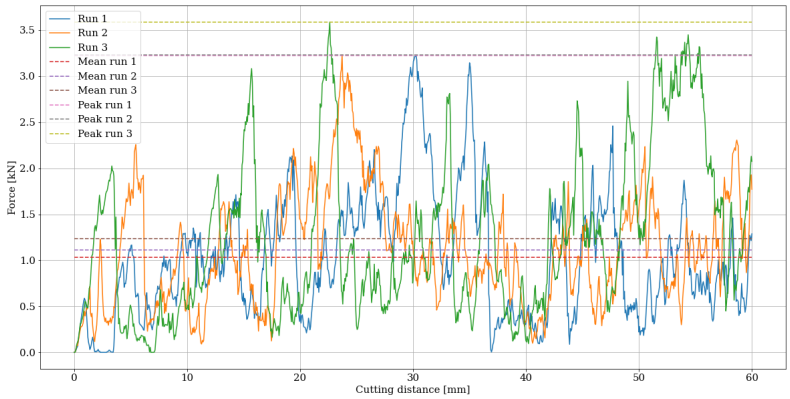

Figure 4.46: Numerical simulation normal force cutting signals for 2 mm cutting depth and skew angle of zero.

Figure 4.47 shows the drag force signals for the three numerical simulation runs at a cutting depth of 2 mm and a skew angle of zero.

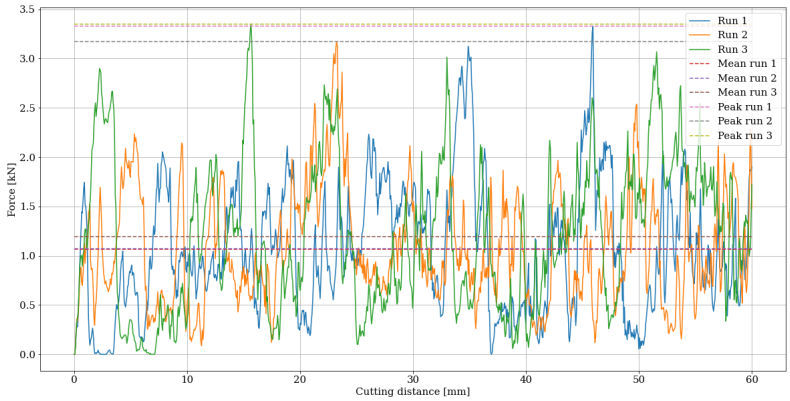

Figure 4.47: Numerical simulation drag force cutting signals for 2 mm cutting depth and skew angle of zero.

Figure 4.48 shows the normal force signals for the three numerical simulation runs at a cutting depth of 4 mm and a skew angle of zero.

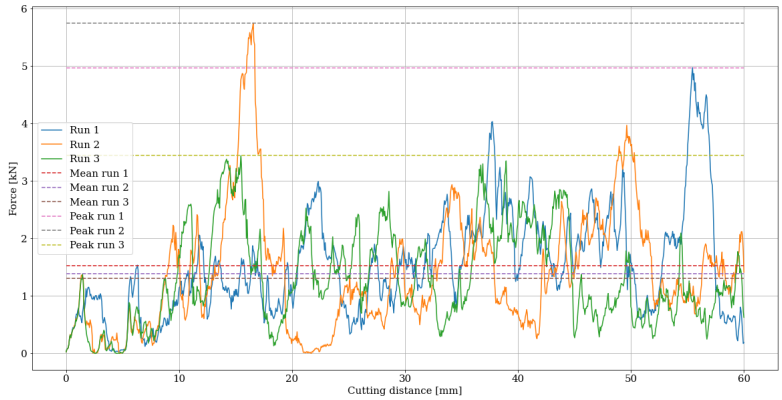

Figure 4.48: Numerical simulation normal force cutting signals for 4 mm cutting depth and skew angle of zero.

Figure 4.49 shows the drag force signals for the three numerical simulation runs at a cutting depth of 4 mm and a skew angle of zero.

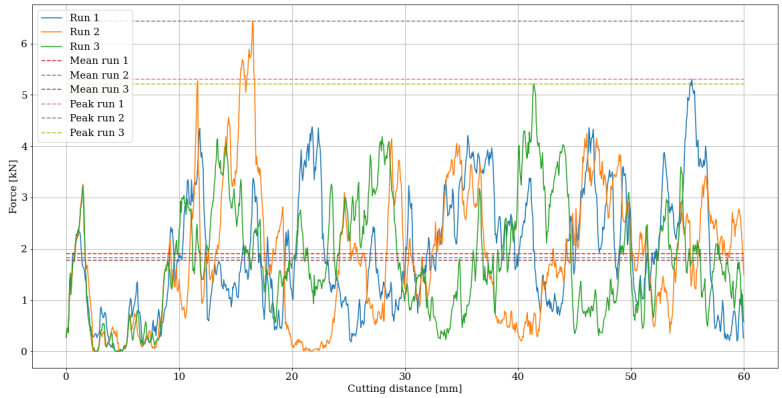

Figure 4.49: Numerical simulation drag force cutting signals for 4 mm cutting depth and skew angle of zero.

Figures 4.46 to 4.49 show how close the mean force and peak force is to one another per run. These figures show that the forces are close to one another as expected from section 2.3.

This section showed that it is possible to use LS-DYNA with the CSCM to model rock cutting of UG2 reef samples and get acceptable results, but the user has to calibrate the model parameters using the experimental results. Thus, the model is only fit for one set of cutting parameters. The section showed that the model does not extrapolate accurately when the cutting parameters are changed.

Chapter 5

Conclusion and recommendations

This final chapter presents the conclusions drawn from the dissertation and recommendations for taking the research forward.

5.1 Conclusion

The literature in section 1.4 illustrated that rock cutting using conical picks is a common method of mining that enables continuous mining operations. Section 1.4.6 showed that various research projects have been conducted on different design aspects using conical picks. None of these studies considered rock samples found in South African hard rock environments. Thus, there was a need for experimental cutting tests on rock samples found in South African hard rock environments, such as UG2 reef samples. These experimental results could then be used to optimize numerical simulation cutting tests model parameters to determine if numerical simulations are able to predict cutting forces accurately when cutting rock samples found in South African hard rock environments. Section 1.4.10 discussed previous research on numerical simulation cutting tests, but there were clear model errors and different rock samples were cut.

The dissertation presents the successful design, manufacturing and testing of a linear cutting machine (LCM). The LCM was required to conduct laboratory scale cutting tests on rock samples, especially rock samples found in South African hard rock environments. Section 3.1 discusses the design, manufacturing and testing of the LCM built for this dissertation. The LCM fulfilled all the requirements needed to conduct the laboratory scale cutting tests so that the results of different types of rock samples can be compared to one another.

Two different rock samples were tested for this dissertation, namely sandstone and UG2 reef samples. Firstly sandstone was cut to ensure that the LCM functions as expected. By cutting sandstone, it ensured that all the kinks of the LCM were fixed. This also gave promising cutting data of material with little to no variance in strength on a millimetre scale, that was compared to the cutting data of the UG2 reef samples. Lastly UG2 reef samples were cut to study the possibility of mechanized mining in hard rock environments. These results were compared to the sandstone results.

The comparison illustrated that there are similarities between the results of the two different rock samples but there are also differences in results. The main difference is that the sandstone has little to no variance in strength on a millimetre scale whereas the UG2 reef sample has large variance in strength on a millimetre scale. A problem of cutting the UG2 reef samples is the inconsistency in rock properties of the UG2 reef. There is a large variance in the material properties as discussed in section 4.1.

The results indicated that the optimal s/d ratio for the different cutting parameters are similar for sandstone and UG2. But the normal force, drag force and specific energy plateaus at a cutting depth of 4 mm for larger s/d values. This implies that the depth of cut has a larger influence on the cutting force results of UG2 reef samples than on sandstone samples. Clearly the sandstone data would not be appropriate to use to make design decisions for mining equipment intended for UG2.

A important difference between cutting sandstone and UG2 reef is the size of the chips formed. At 2 mm cutting depth for both rock samples, the force signals were impulsive and the material gathered was fine fragmentations. But at a cutting depth of 4 mm for both samples the force signals had a saw tooth shape. This implies larger chips that are formed. The sandstone did produce large chips whereas the UG2 produced fine fragmentations. This fine fragmentations is undesirable in underground mining conditions owing to the difficulty of cleaning this from the stopes.

Using fast Fourier transform (FFT) analysis is a useful method to discuss and compare rock cutting data. Valuable information can be obtained when looking at the FFT analysis, such as if the cutting force signal is periodic and the size of the chips formed. In this dissertation, section 4.3 showed that from the FFT, of the sandstone data, it is clear that the drag force signal is periodic and that clear conclusions can be drawn about the size of the chips formed at the different cutting depths. For the UG2 however the conclusions are not so clear. Owing to the UG2 not being periodic, because of the UG2 having large variance in strength on a millimetre scale, the FFT analysis do not give useful information about the size of the chips formed.

The numerical simulations illustrated that there are various model parameters that influences the results and some that do not influence the results. Some parameters are based on material properties and other are updated through trial and error. The parameters are updated by changing model parameters and the material properties, used in the equations given by (Novozhilov, Dmitriev and Mikhaluk, 2022) as discussed in sections 2.2 and 4.4, until an acceptable accuracy is obtained between the numerical simulation cutting results and the experimental cutting results for a constant set of cutting parameters.

It is possible to model rock cutting of UG2 reef samples using LS-DYNA and the CSCM. But this is only possible by updating the model parameters through trial and error for one set of cutting parameters. When the cutting parameters are changed, such as the cutting depth, the model does not give acceptable results. Thus, the model is not capable of extrapolation.

In conclusion, the dissertation confirmed the possible use of conical picks for mechanized mining in

hard rock environments such as UG2 reef, however it will be problematic as its fragmentation will be too fine. It was also shown that it is possible to simulate the cutting process using FEM software. However, the model does not give good results when extrapolating beyond the specific conditions considered to obtain the rock characteristics, for example for different cut depths.

5.2 Recommendations

From the results of the laboratory scale cutting tests of the UG2 reef samples it is clear that the material has large variance in strength on a millimetre scale. Therefore more tests should be conducted on different samples of UG2 reef found in other parts of the mine or different parts of the Bushveld complex. The influence on the FFT results should also be investigated. The relationship between cycles and chips formed, when cutting rock samples, should also be investigated further using FFT analysis.

The results of the laboratory scale cutting tests should be compared to new cutting test results obtained form cutting other rock types found in hard rock environments such as Merensky reef samples. This would highlight the similarities and differences in cutting the different rock types. It will also provide insight into the variance in strength on a millimetre scale of the rock and the cut-ability of other rock types.

Different types of picks can be investigated such as radial picks, which is the second most common drag/pick tool as discussed in section 1.4.6. Also discussed in section 1.4.4 is tool ware, an important aspect of the efficiency of the tool, thus of the equipment and thus of the mine itself. Research should be conducted to investigated if current conical picks can be used on new low profile cutting equipment or will new picks have to be developed when mining rock found in South African hard rock environments to ensure that the tool wear is not a problem for the efficiency of the mining equipment.

Using FFT analysis is an area of analysing rock cutting data that should be investigated further. This method of analysis might give a better understanding of the cutting process and the relationship between the shape of the cutting force signal and the size of the chips formed.

For the numerical simulation, the model was able to predict cutting forces, at a cutting depth of 2 mm, with encouraging accuracy. But it did not generalize well to different cutting depths as seen in section 4.4 where the percentage error of the predicted cutting forces, at a cutting depth of 4 mm, are on average 40%. While this is not ideal at all, it is important to realise that if one considers the experimental runs them self, they had an average error for the mean force of 15% and 11% for the peak forces. But further investigation can be conducted to determine better model parameters using the CSCM in LS-DYNA.

In the present work the rock model parameters were determined on the basis of cutting experiments at specific cutting depths. Future work should investigate the use of characteristics obtained from experiments over a range of cutting depths to obtain more representative characteristics. Other material models can also be investigated or other FEM software. DEM software can also be investigated

to determine if DEM simulations will give better results than FEM simulations when extrapolating.

Bibliography

Artstation, 2020. *3d nora tunnel boring machine* [Online]. 3D model. Available from: `https://www.artstation.com/artwork/mqkmke`.

Bilgin, N., Demircin, M.A., Copur, H., Balci, C., Tuncdemir, H. and Akcin, N., 2006. Dominant rock properties affecting the performance of conical picks and the comparison of some experimental and theoretical results. *International Journal of Rock Mechanics and Mining Sciences*, 43 (1), pp.139–156.

Bilgin, N., Copur, H. and Balci, C., 2013. *Mechanical Excavation in Mining and Civil Industries*. Boca Raton.

Copur, H., Bilgin, N., Balci, C., Tumac, D. and Avunduk, E., 2017. Effects of different cutting patterns and experimental conditions on the performance of a conical drag tool. *Rock Mechanics and Rock Engineering*, 50 (6), pp.1585–1609.

Dehkhoda, S. and Detournay, E., 2019. Rock cutting experiments with an actuated disc. *Rock Mechanics and Rock Engineering*, 52 (9), pp.3443–3458.

Evans, I., 1962. A theory of the basic mechanics of coal ploughing. *Proceedings of the International Symposium on Mining Research*, 2 (1), pp.761–768.

Fourie, F., Valicek, P., Krafft, G. and Sevenoaks, J., 2014. Narrow reef mechanised mining layout at Anglo American Platinum. . *The 6th International Platinum Conference, 'Platinum–Metal for the Future'*.

Hekimoglu, O.Z., 2018. Investigations into tilt angles and order of cutting sequences for cutting head design of roadheaders. *Tunnelling and Underground Space Technology*, 76, pp.160–171.

Höll, H., 2009. *Pillar Design and Cutting at Everest Platinum Mine*. (technical report). Aquarius Platinum (South Africa) (Pty) Ltd.

Huang, J., Zhang, Y., Zhu, L. and Wang, T., 2016. Numerical simulation of rock cutting in deep mining conditions. *International Journal of Rock Mechanics and Mining Sciences*, 84, pp.80–86.

Jaime, M.C., Zhou, Y., Lin, J.-S. and Gamwo, I.K., 2015. *Finite Element Modeling of Rock Cutting and its Fragmentation Process*. Department of Civil and Environmental Engineering, University of Pittsburgh, Pittsburgh, PA, USA.

Jaime, M.C., 2011. *Numerical modeling of rock cutting and its associated fragmentation process using the finite element method*. University of Pittsburgh Swanson School of Engineering.

Kalogeropoulos, A. and Michalakopoulos, T., 2021. Numerical simulation of rock cutting using YADE. *Matec web of conferences*, 342, p.02011.

Kang, H., Cho, J.-W., Park, J.-Y., Jang, J.-S., Kim, J.-H., Kim, K.-W., Rostami, J. and Lee, J.-W., 2016. A new linear cutting machine for assessing the rock-cutting performance of a pick cutter. *International Journal of Rock Mechanics and Mining Sciences*, 88, pp.129–136.

Kotwica, K. and Gospodarczyk, P., 2003. Hard rock mining with the use of new cutting tools. *Journal of Mining Science*, 39.

Kotwica, K., 2019. Hard rock mining-cutting or disk tools. Vol. 545. Institute of Physics Publishing.

Kotwica, K., 2018. Atypical and innovative tool, holder and mining head designed for roadheaders used to tunnel and gallery drilling in hard rock. *Tunnelling and Underground Space Technology*, 82, pp.493–503.

Li, B., Zhang, B., Hu, M., Liu, B., Cao, W. and Xu, B., 2022. Full-scale linear cutting tests to study the influence of pre-groove depth on rock-cutting performance by TBM disc cutter. *Tunnelling and Underground Space Technology*, 122.

Liu, S., Zhou, F., Li, H., Chen, Y., Wang, F. and Guo, C., 2020. Experimental investigation of hard rock breaking using a conical pick assisted by abrasive water jet. *Rock Mechanics and Rock Engineering*, 53 (9), pp.4221–4230.

Mendyka, P., 2017. Laboratory stand tests of mining asymmetrical disc tools. *17th International Multidisciplinary Scientific GeoConference SGEM 2017*. Section Exploration and Mining.

Moxham, K.A., 2004. A narrow reef mining machine - arm1100. *International Platinum Conference 'Platinum Adding Value'*.

Nishimatsu, Y., 1997. The mechanics of rock cutting. *International Journal of Rock Mechanics and Mining Sciences and Geomechanics Abstracts*, 9 (1), pp.261–271.

Novozhilov, Y.V., Dmitriev, A.N. and Mikhaluk, D.S., 2022. *Precise Calibration of the Continuous Surface Cap Model for Concrete Simulation*. Buildings.

Ozdemir, L., 1977. *Development of theoretical equations for predicting tunnel boreability*. (Thesis). Dempartment of Mining Engineering, Colorado School off Mines.

Park, J.Y., Kang, H., Lee, J.W., Kim, J.H., Oh, J.Y., Cho, J.W., Rostami, J. and Kim, H.D., 2018. A study on rock cutting efficiency and structural stability of a point attack pick cutter by lab-scale linear cutting machine testing and finite element analysis. *International Journal of Rock Mechanics and Mining Sciences*, 103, pp.215–229.

Pickering, R.G.B., 2007. Has the South African narrow reef mining industry learnt how to change? *The Journal of The Southern African Institute of Mining and Metallurgy*, 107, pp.557–565.

Sandvik, 2015. *Mechanical cutting* [Online]. Brochure. Available from: `https://pdf.directindustry.com/pdf/sandvik-mining-rock-technology/sandvik-mechanical-cutting/40142-599928.html`.

Sandvik, 2022. *Sandvik conical and radial picks* [Online]. Brochure. Available from: https://www.rocktechnology.sandvik/en/products/rock-tools/cutting/cutting-tools/conical-and-radial-picks/.

Sifferlinger, N.A., Hartlieb, P. and Moser, P., 2017. The importance of research on alternative and hybrid rock extraction methods. *BHM Berg- und Hüttenmännische Monatshefte*, 162 (2), pp.58–66.

Stopka, G., 2021. Modelling of Rock Cutting with Asymmetrical Disc Tool Using Discrete-Element Method (DEM). *Rock Mechanics and Rock Engineering*, 54 (12), pp.6265–6279.

Su, O. and Akcin, N.A., 2011. Numerical simulation of rock cutting using the discrete element method. *International Journal of Rock Mechanics and Mining Sciences*, 48 (3), pp.434–442.

Tools, E.M., 2022. *Conical pick* [Online]. Brochure. Available from: https://www.emtsa.co.za/product/conical-pick-35mm-shank/.

Trentacoste, M., 2007. *Users Manual for LS-DYNA Concrete*.

Van Wyk, G., Els, D.N., Akdogan, G., Bradshaw, S.M. and Sacks, N., 2014. Discrete element simulation of tribological interactions in rock cutting. *International Journal of Rock Mechanics and Mining Sciences*, 65, pp.8–19.

Vogt, D., 2016. A review of rock cutting for underground mining: past, present, and future. *Journal of the Southern African Institute of Mining and Metallurgy*, 116 (11), pp.1011–1026.

Wicaksana, Y., Jeong, H. and Jeon, S., 2021. Numerical simulation of rock cutting process induced by a pick cutter considering dynamic properties of rock at intermediate strain rate. *Bulletin of Engineering Geology and the Environment*, 80 (12), pp.9049–9069.

Zárate, F. and Oñate, E., 2015. A simple FEM–DEM technique for fracture prediction in materials and structures. *Computational Particle Mechanics*, 2 (3), pp.301–314.

Zou, J., Yang, W. and Han, J., 2020. Discrete element modeling of the effects of cutting parameters and rock properties on rock fragmentation. *IEEE Access*, 8, pp.136393–136408.

Appendix

A Drag force colour maps for sandstone

Figure A.1 shows the drag force map for cutting sandstone at 2 mm cutting depth with skew angle 0°.

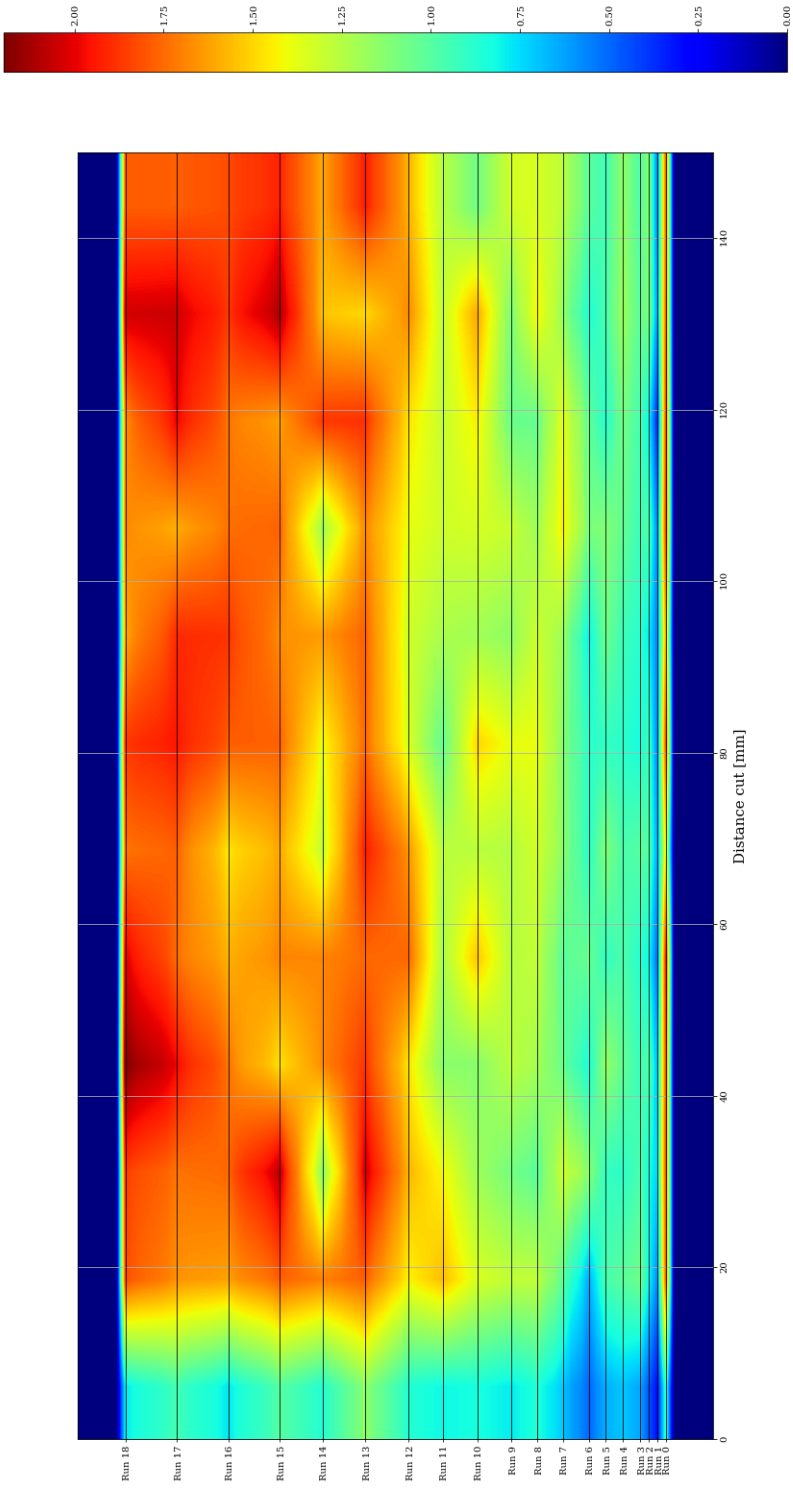

Figure A.1: Drag force mapping of sandstone at skew angle = 0°.

Figure A.2 shows the drag force map for cutting sandstone at 2 mm cutting depth with skew angle $-10°$.

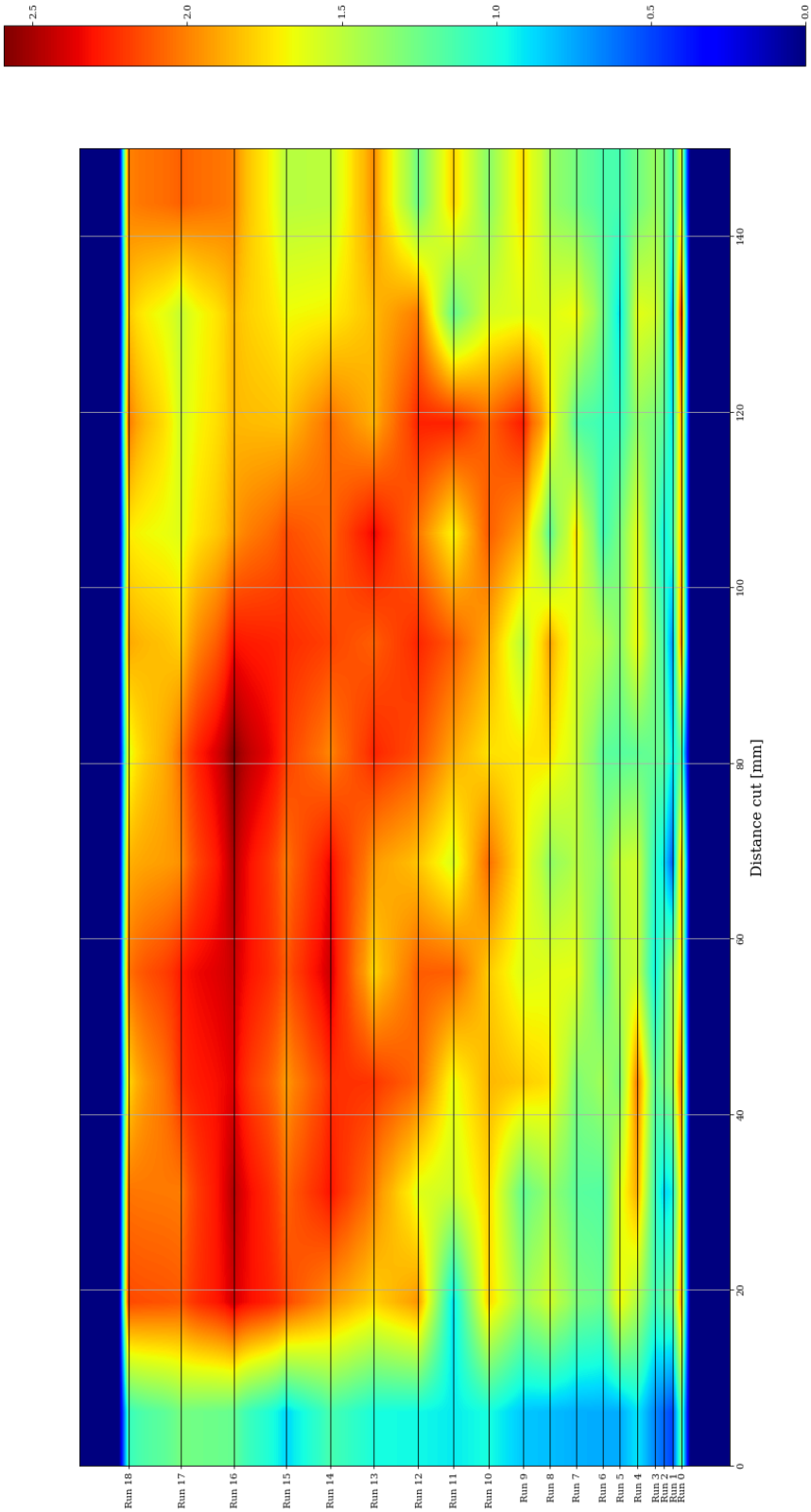

Figure A.2: Drag force mapping of sandstone at skew angle = $-10°$.

Figure A.3 shows the drag force map for cutting sandstone at 2 mm cutting depth with skew angle $+10°$.

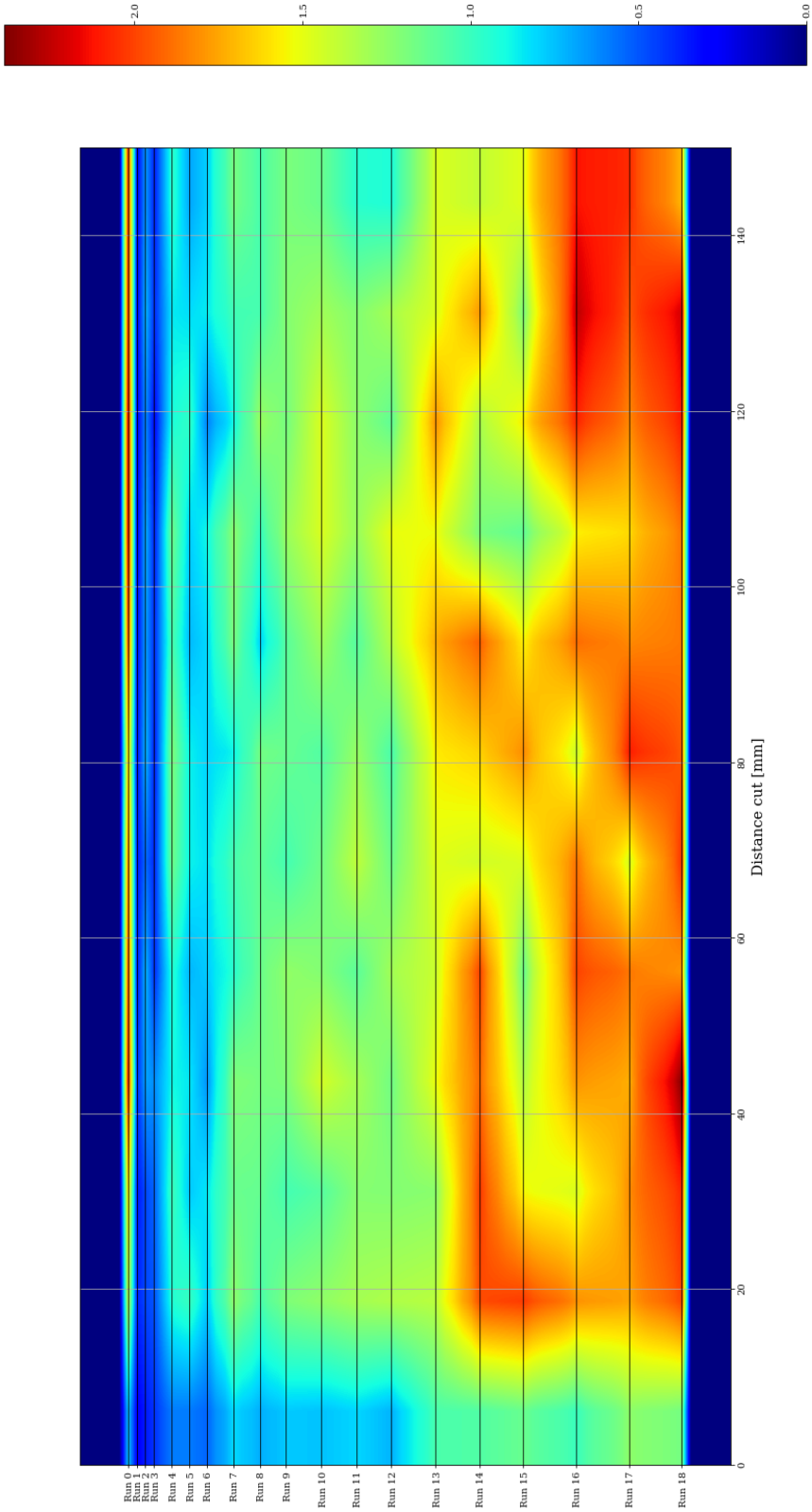

Figure A.3: Drag force mapping of sandstone at skew angle = $+10°$.

B Drag force colour maps for UG2

Figure B.1 shows the drag force map for cutting UG2 at 2 mm cutting depth with skew angle 0°.

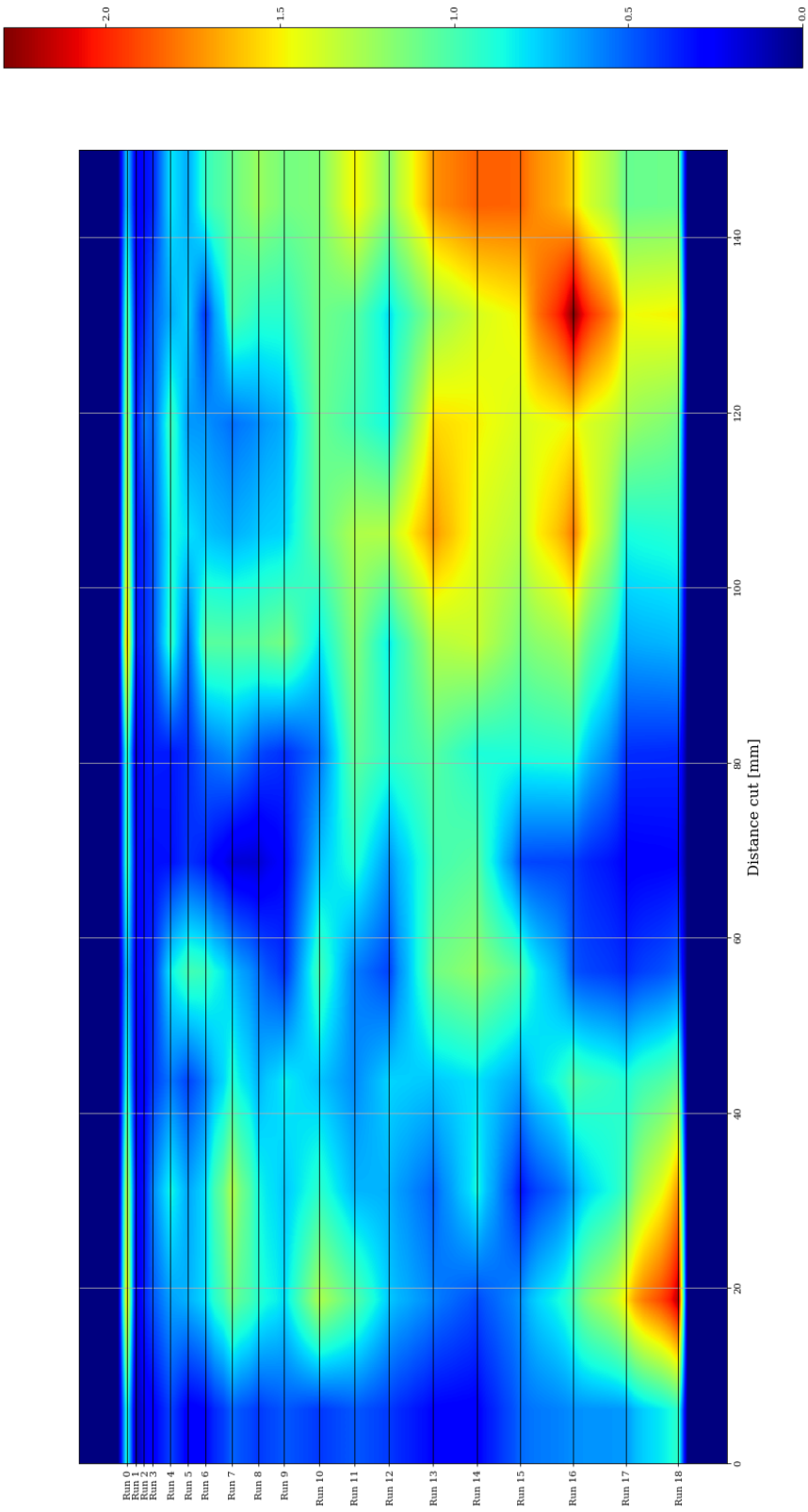

Figure B.1: Drag force mapping of UG2 at skew angle = 0°.

Figure B.2 shows the drag force map for cutting UG2 at 2 mm cutting depth with skew angle $-10°$.

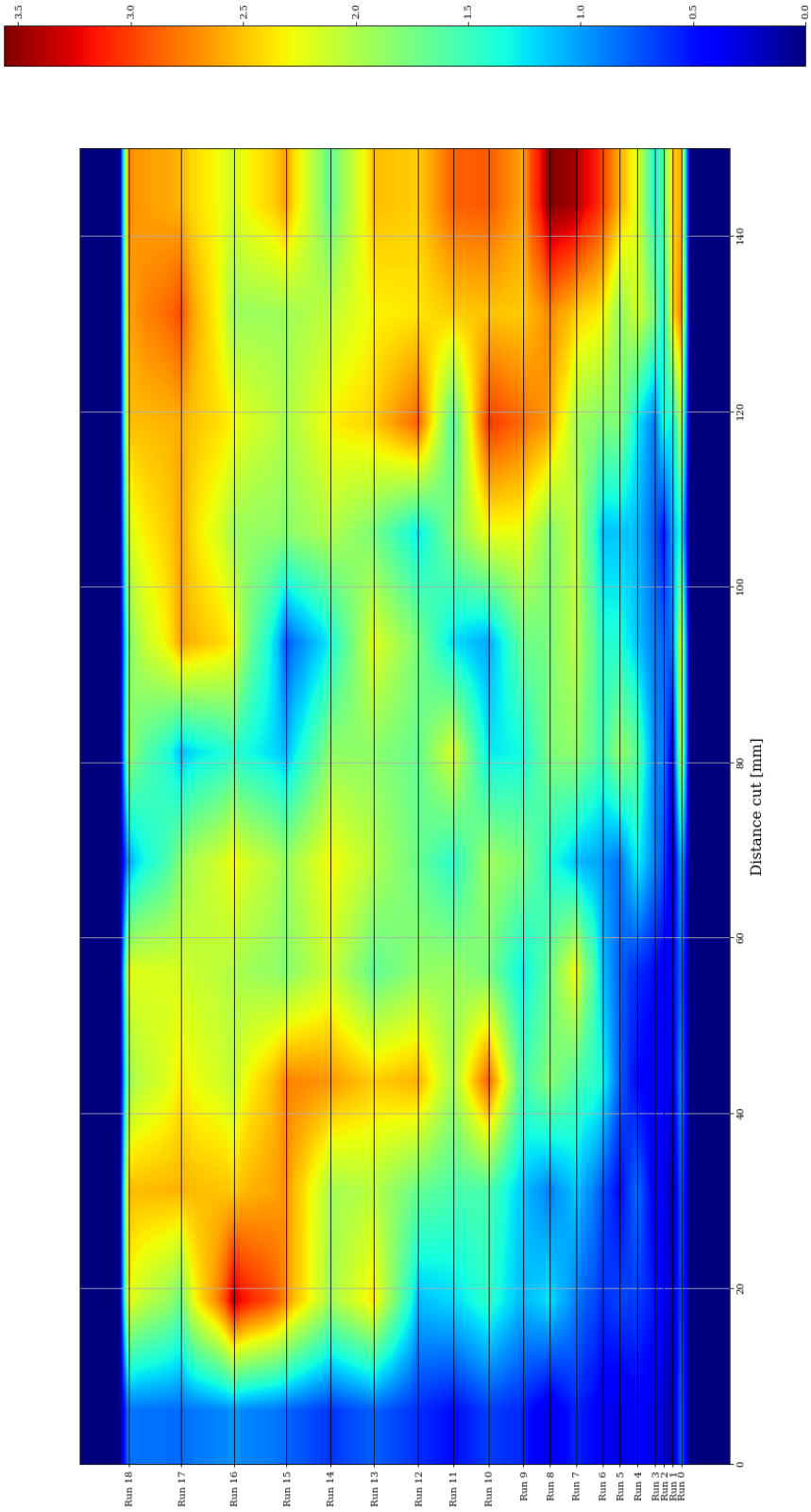

Figure B.2: Drag force mapping of UG2 at skew angle = $-10°$.

Figure B.3 shows the drag force map for cutting UG2 at 2 mm cutting depth with skew angle $+10°$.

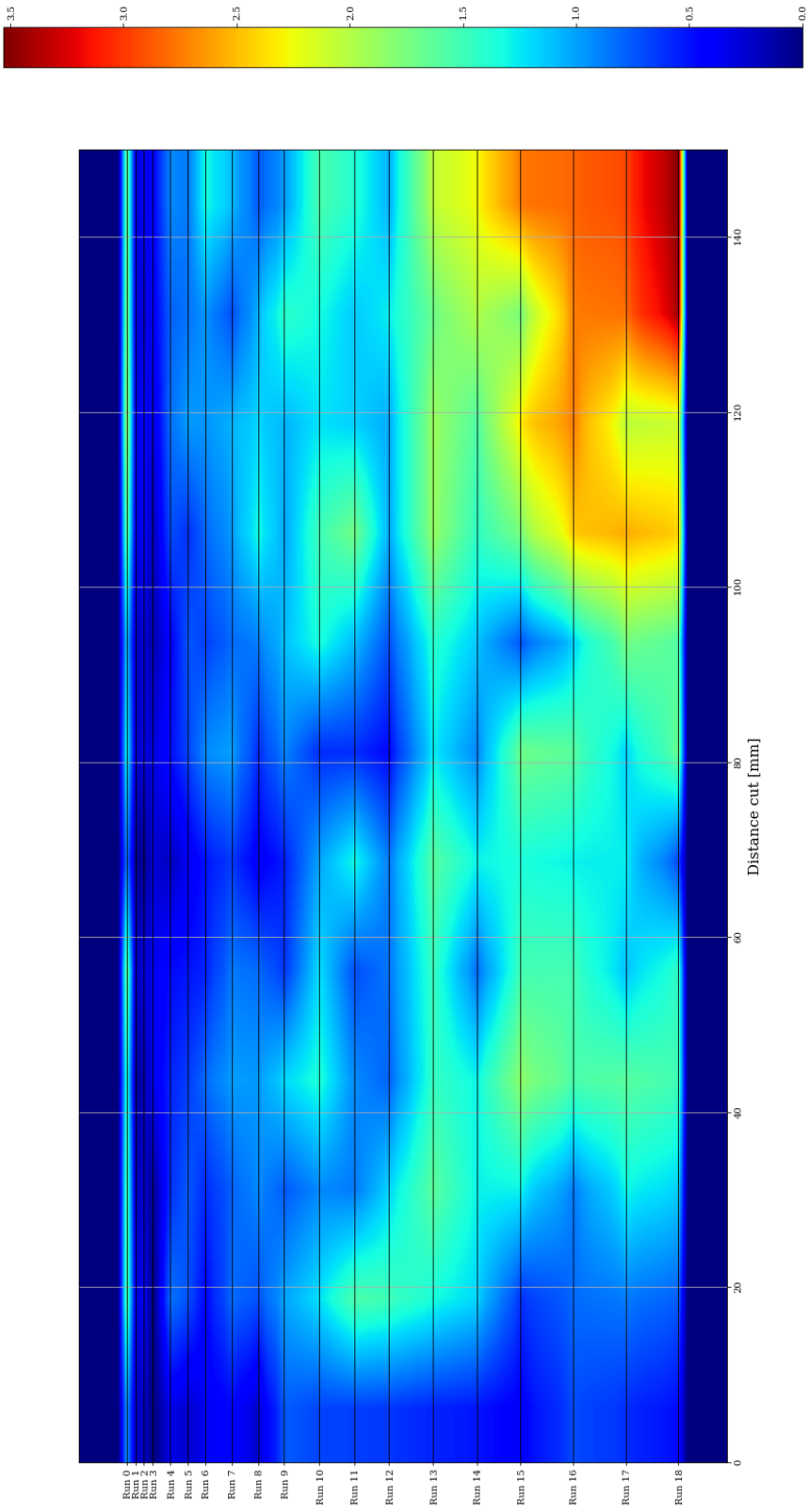

Figure B.3: Drag force mapping of UG2 at skew angle = $+10°$.

C Normalized drag force colour maps for UG2

Figure C.1 shows the normalized drag force map for cutting UG2 at 2 mm cutting depth with skew angle 0°.

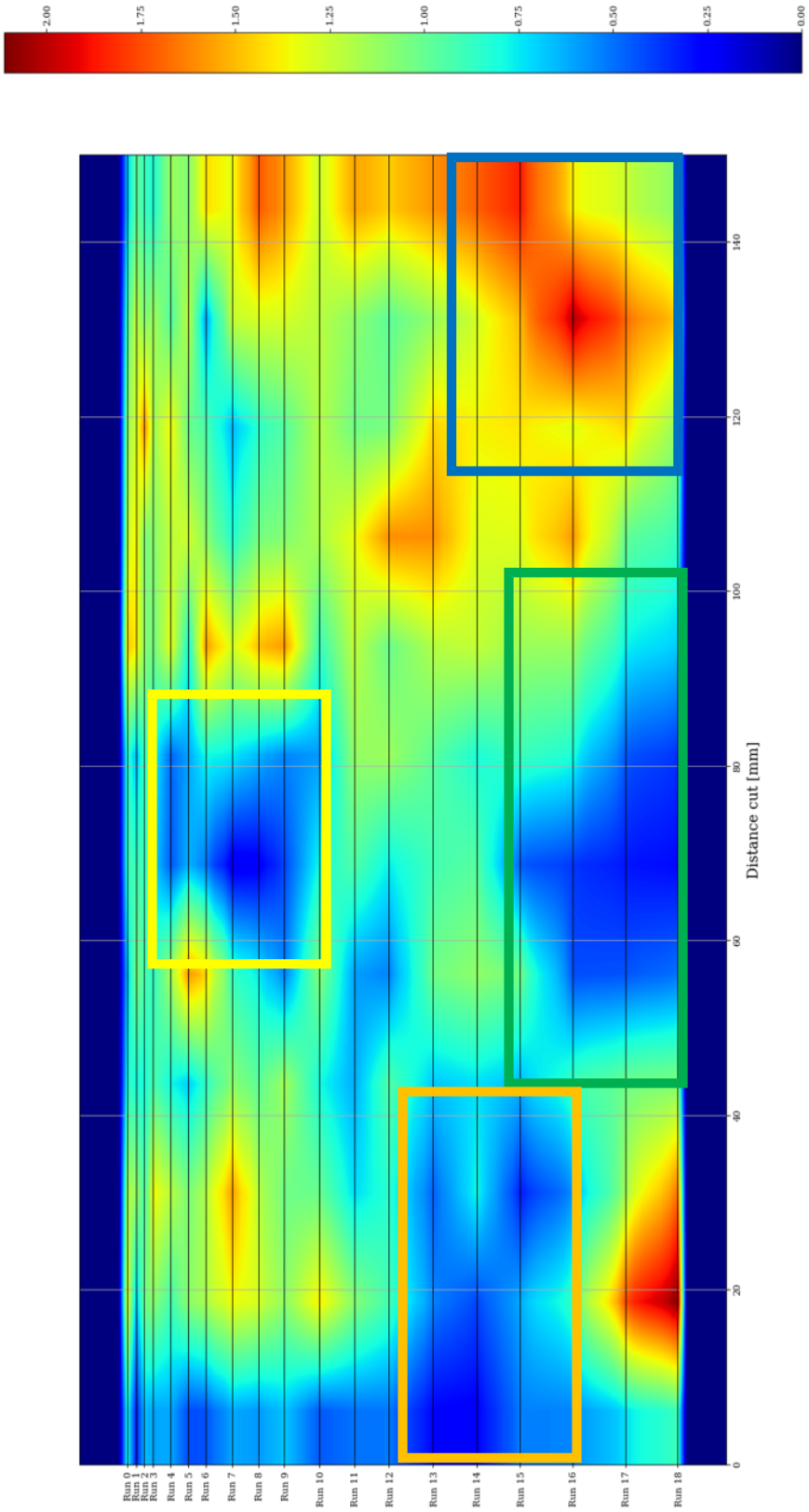

Figure C.1: Normalized drag force mapping of UG2 at skew angle = 0°.

Figure C.2 shows the normalized drag force map for cutting UG2 at 2 mm cutting depth with skew angle $-10°$.

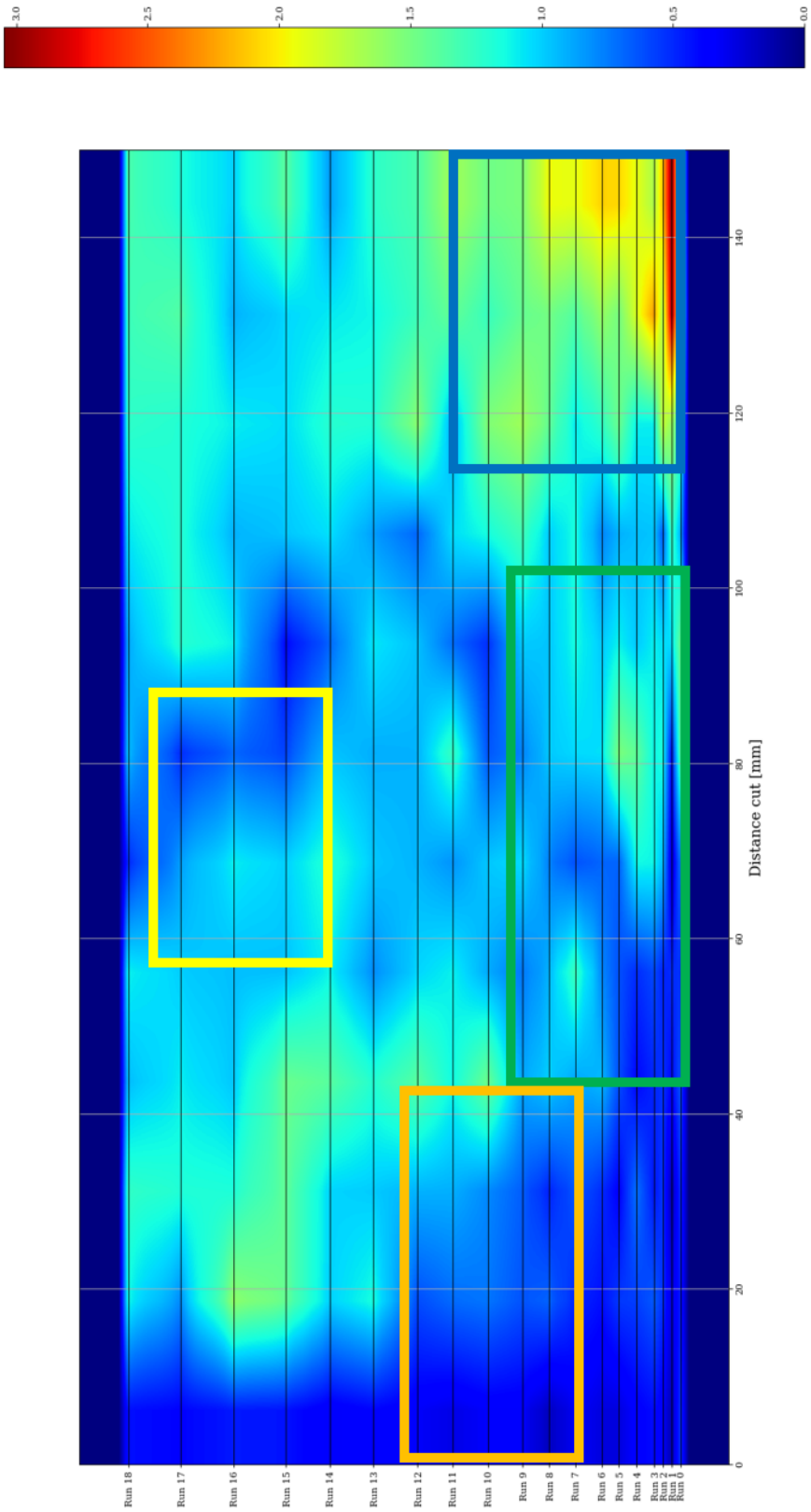

Figure C.2: Normalized drag force mapping of UG2 at skew angle = $-10°$.

Figure C.3 shows the normalized drag force map for cutting UG2 at 2 mm cutting depth with skew angle $+10°$.

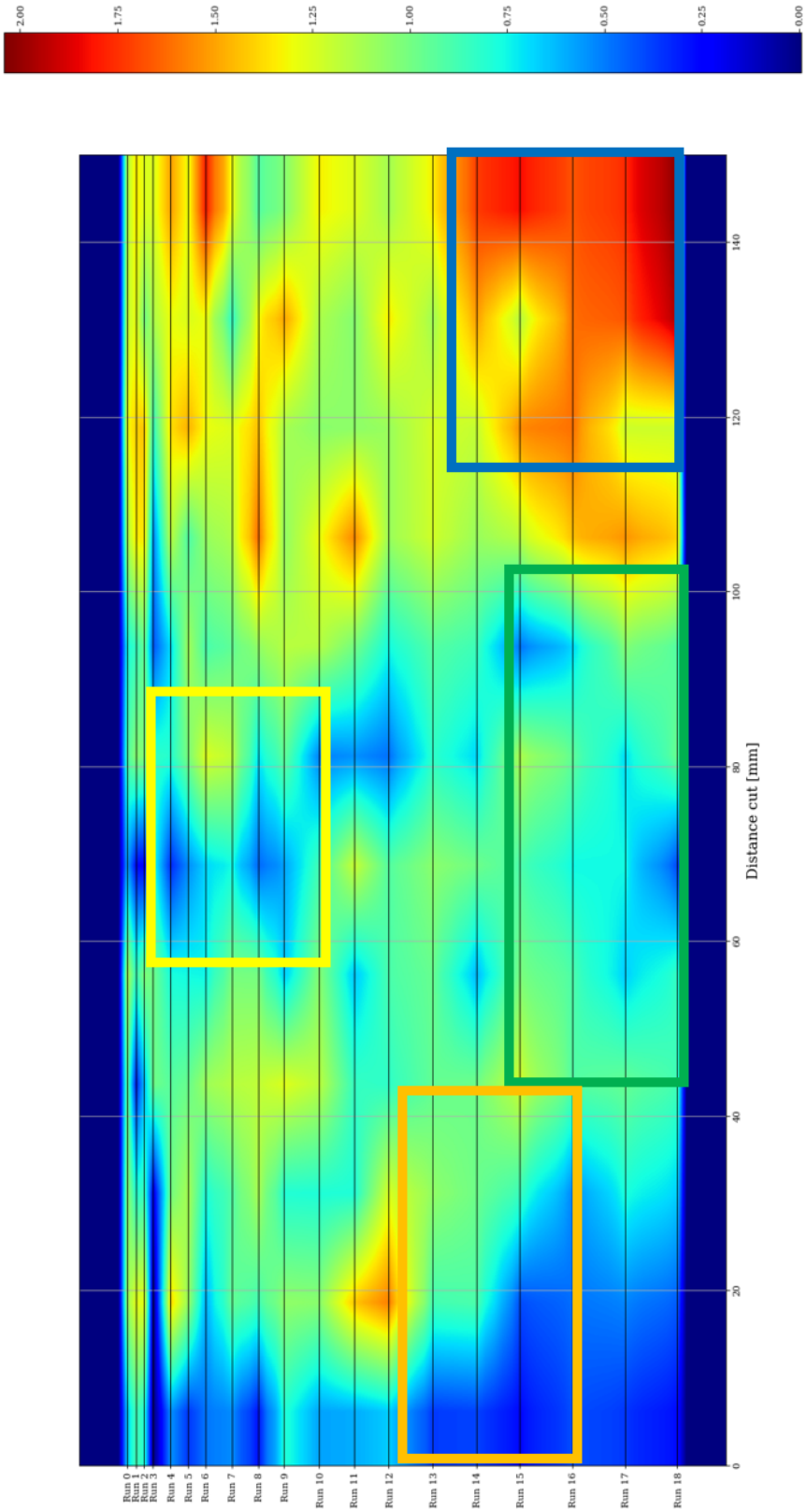

Figure C.3: Normalized drag force mapping of UG2 at skew angle = $+10°$.

D Side force colour maps for sandstone

Figure D.1 shows the side force map for cutting sandstone at 2 mm cutting depth with skew angle 0°.

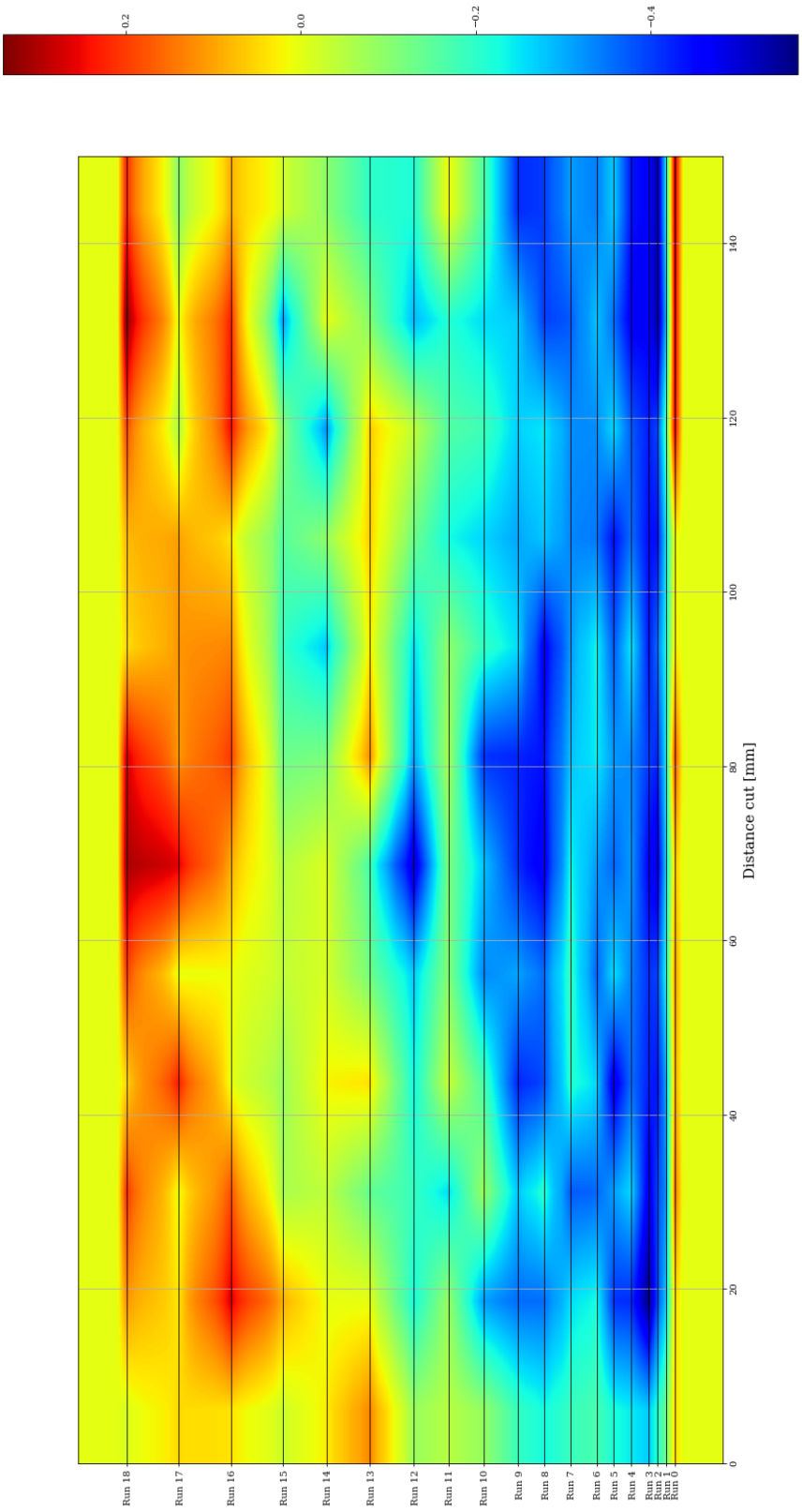

Figure D.1: Side force mapping of sandstone at skew angle = 0°.

Figure D.2 shows the side force map for cutting sandstone at 2 mm cutting depth with skew angle $-10°$.

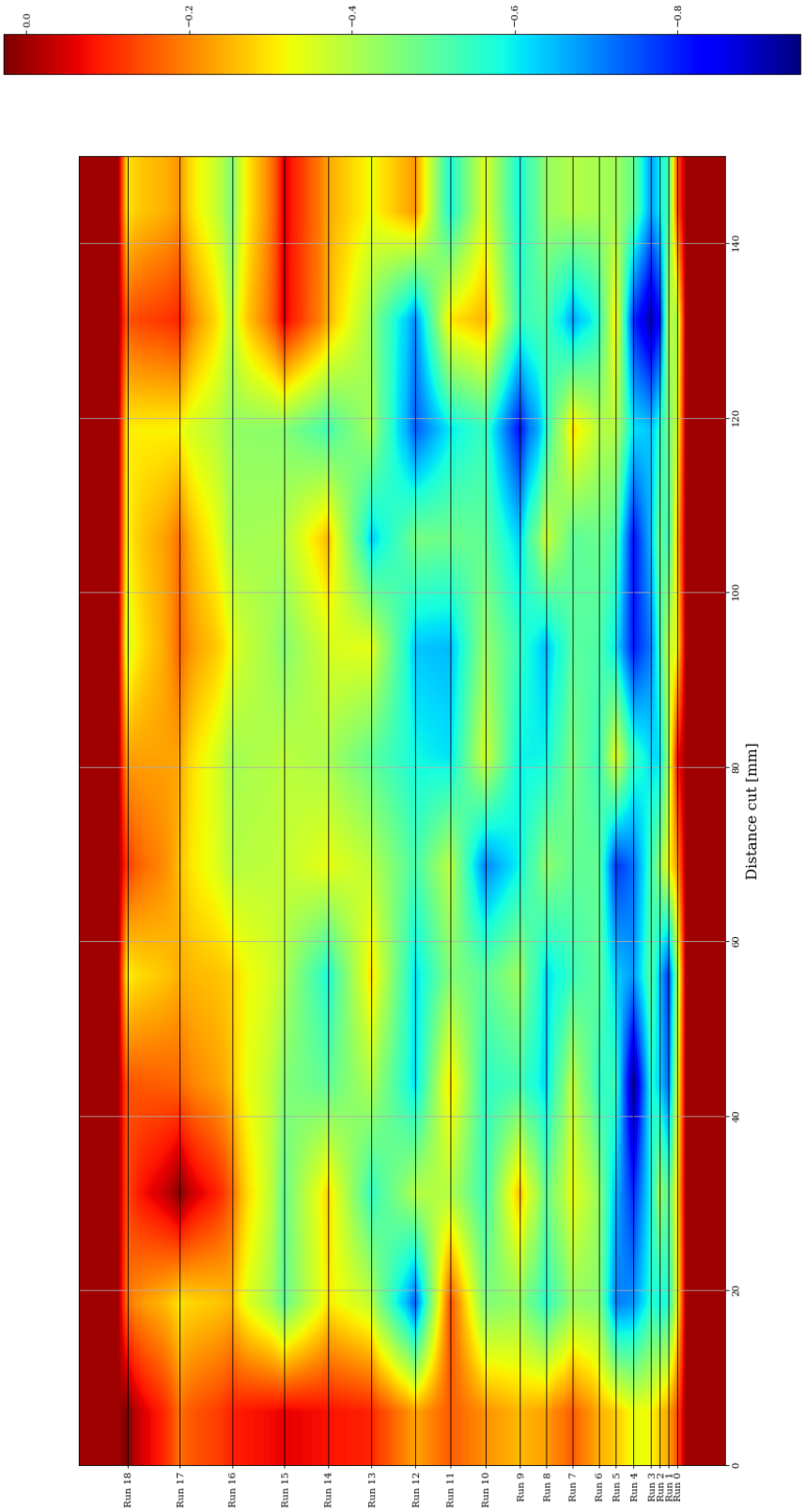

Figure D.2: Side force mapping of sandstone at skew angle = $-10°$.

Figure D.3 shows the side force map for cutting sandstone at 2 mm cutting depth with skew angle $+10°$.

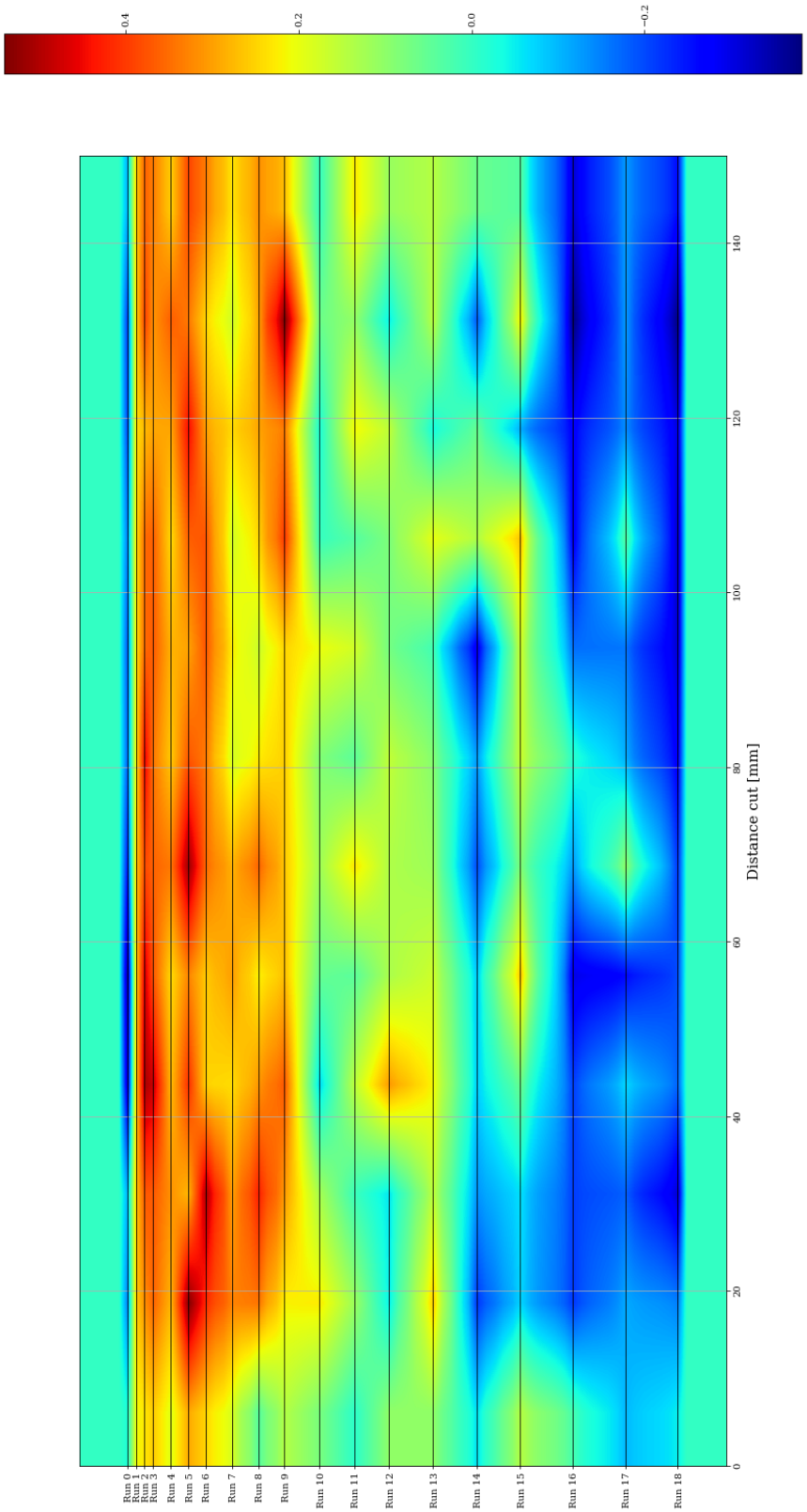

Figure D.3: Side force mapping of sandstone at skew angle = $+10°$.

E Side force colour maps for UG2

Figure E.1 shows the side force map for cutting UG2 at 2 mm cutting depth with skew angle 0°.

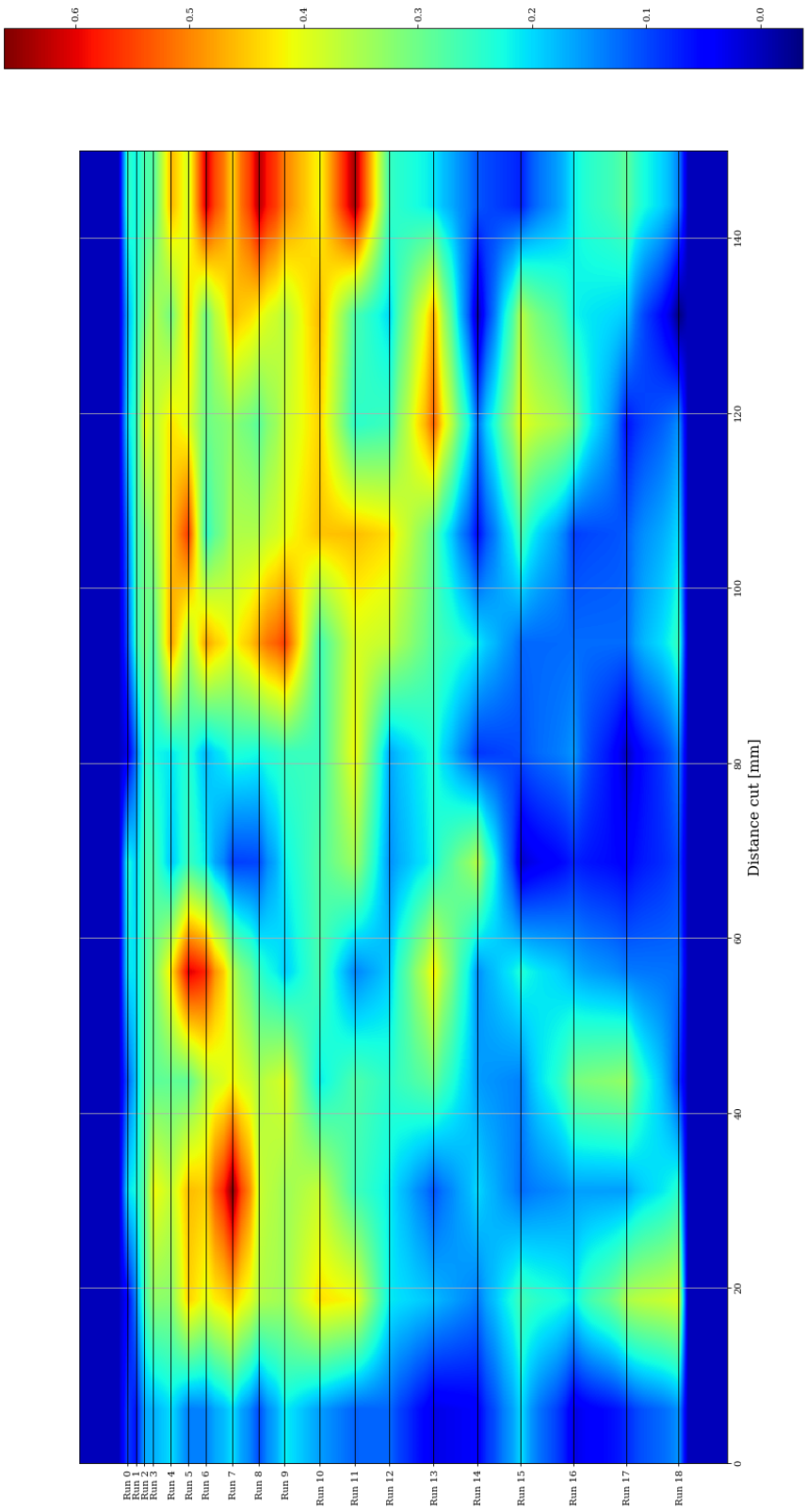

Figure E.1: Side force mapping of UG2 at skew angle = 0°.

Figure E.2 shows the side force map for cutting UG2 at 2 mm cutting depth with skew angle $-10°$.

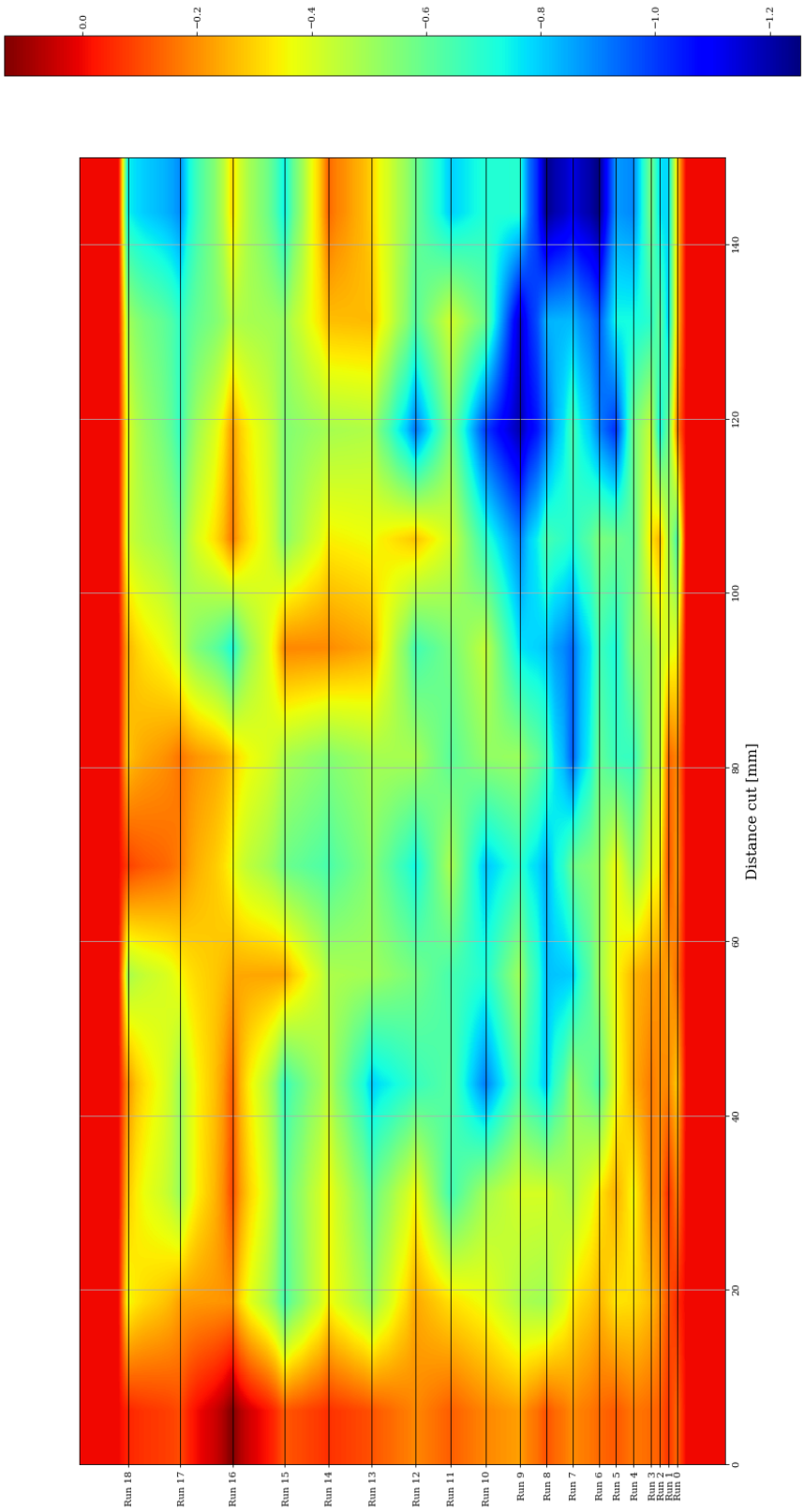

Figure E.2: Side force mapping of UG2 at skew angle = $-10°$.

Figure E.3 shows the side force map for cutting UG2 at 2 mm cutting depth with skew angle $+10°$.

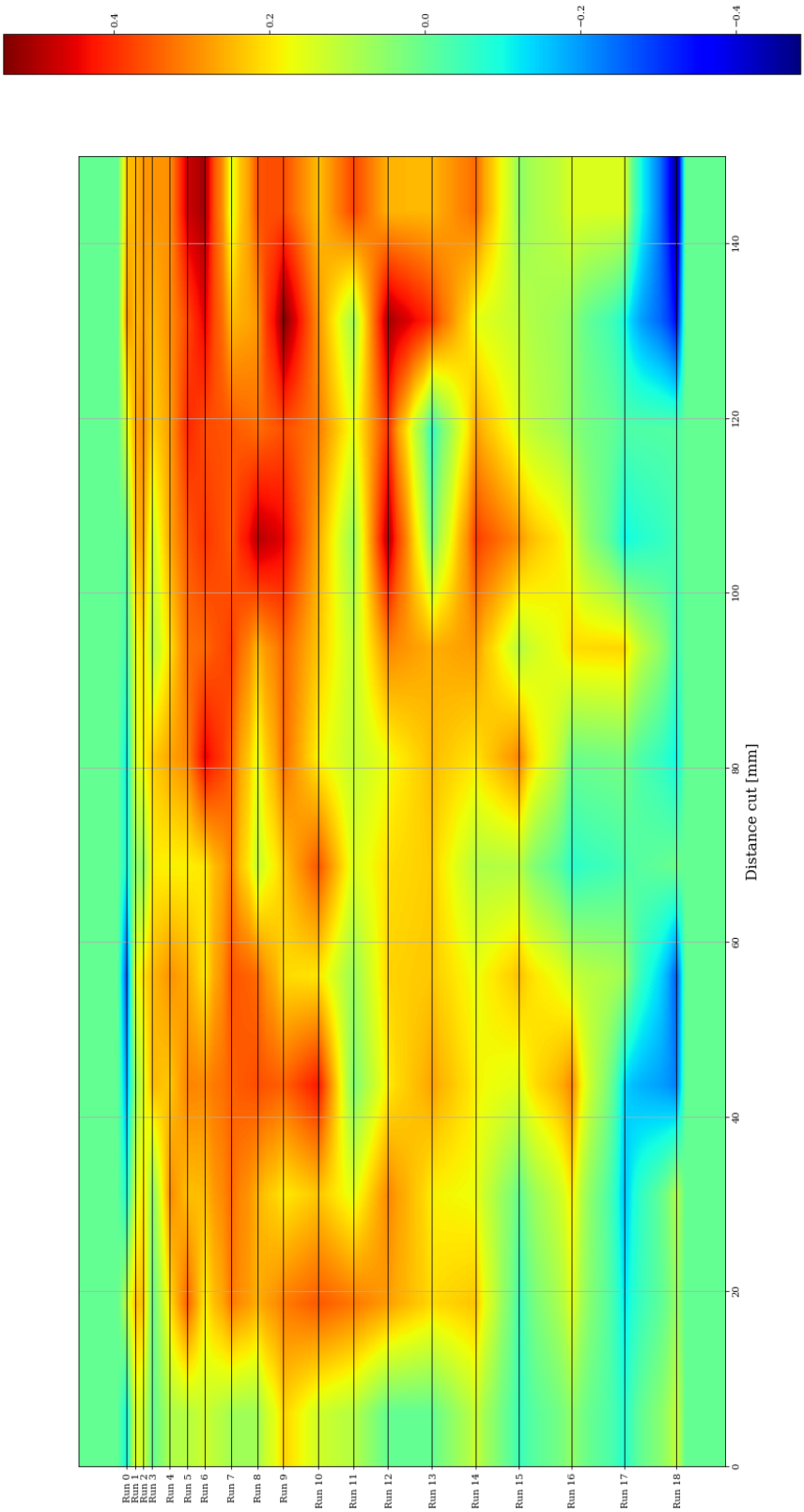

Figure E.3: Side force mapping of UG2 at skew angle = $+10°$.